

Study of Zinc Ferrite/Graphene Oxide nanocomposites

A Dissertation Report for

Course code and Course Title: PHGO-311 Dissertation

Credits: 8

Submitted in partial fulfilment of Master's Degree

M.Sc. in Physics/ Solid State Physics

by

SHREYA RAMDAS KARKADE

Roll Number: 21P043025

PRATIK NARAYAN BODNEKAR

Roll Number: 21P043005

Under the Supervision of

DR. PRANAV P. NAIK

School of Physical and Applied Sciences
Physics



GOA UNIVERSITY

Date: May 2023



Seal of the School

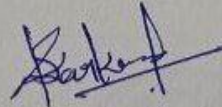
Examined by:

Praveen
Pravin
Pravin
Pravin
Pravin
Pravin

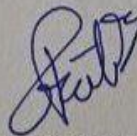
DECLARATION BY STUDENT

I hereby declare that the data presented in this Dissertation report entitled, "Study of Zinc Ferrite/ Graphene Oxide nanocomposites" is based on the results of investigations carried out by us in the Physics Department at the School of Physical and Applied Sciences, Goa University under the Supervision of Dr. Pranav P. Naik and the same has not been submitted elsewhere for the award of a degree or diploma by us. Further, we understand that Goa University or its authorities will be not be responsible for the correctness of observations / experimental or other findings given the dissertation.

I hereby authorize the University authorities to upload this dissertation on the dissertation repository or anywhere else as the UGC regulations demand and make it available to any one as needed.



Shreya Ramdas Karkade
Roll Number: 21P043025



Pratik Narayan Bodnekar
Roll Number: 21P043005

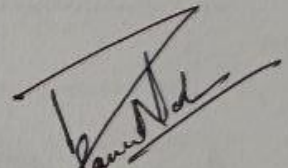
School of Physical and Applied
Sciences

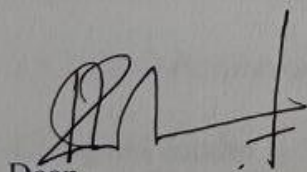
Date: May 2023

COMPLETION CERTIFICATE

This is to certify that the dissertation "**Study of Zinc Ferrite/ Graphene Oxide nanocomposites**" is a bonafide work carried out by **Ms. Shreya Ramdas Karkade & Mr. Pratik Narayan Bodnekar** under my supervision in partial fulfilment of the requirements for the award of the degree of **M.Sc.** in the Discipline Physics at the School of Physical and Applied Sciences, Goa University.

Date: 30/05/2023


Guide



Dean
School Stamp
School of Physical and Applied Sciences



Date: May 2023
Place: Goa University

CONTENTS

DECLARATION BY STUDENT	ii
COMPLETION CERTIFICATE	iii
CONTENT	iv
LIST OF ILLUSTRATIONS	viii
ABSTRACT	1
CHAPTER 1: INTRODUCTION	2
1.1 Energy Storage Systems	2
1.1.1 Classification of energy storage	2
1.1.2 Emerging technologies	6
1.2 Nanomaterials, Nanoparticles, Nanotechnology and Nanocomposites	6
1.3 Nanocomposites in energy storage applications	7
1.4 Ferrites in energy storage application	8
1.5 Ferrites	9
1.5.1 Classification of ferrites	9
1.6 Spinel Oxides	12
1.7 Spinel Ferrites	12
1.8 Zinc Ferrite	14
1.9 Graphene Oxide	14
1.10 Aim of Present Study	15
1.11 Literature review	16
1.12 References	26
CHAPTER 2: METHODS OF MATERIAL PREPARATION	30
2.1 Methods of preparation of ferrite nanoparticles	30

2.1.1 Co-precipitation method	30
2.1.2 Spray pyrolysis method	31
2.1.3 Sol-Gel method	33
2.1.4 High Energy Ball Milling method	34
2.1.5 Combustion method	36
2.1.6 Hydrothermal method	37
2.2 Methods of preparation of Graphene Oxide nanoparticles	40
2.2.1 Hofmann's Method	40
2.2.2 Staudenmaier's Method	41
2.2.3 Tour's Method	42
2.2.4 Modified Hummer's Method	43
2.3 Method of preparation of Zinc Ferrite-Graphene Oxide nanocomposite	46
2.4 Glimpses of the sample preparation process	47
2.5 References	49
CHAPTER 3: CHARACTERISATION TECHNIQUES	52
3.1 X-ray Powder Diffraction	52
3.1.1 Introduction	52
3.1.2 Basic Principle	52
3.1.3 Instrumentation	54
3.2 Scanning Electron Microscopy	55
3.2.1 Introduction	55
3.2.2 Basic Principle	56
3.2.3 Instrumentation	56
3.3 UV-Visible Spectroscopy	57
3.3.1 Introduction	57

3.3.2 Basic principle	58
3.3.3 Instrumentation	59
3.4 The Superconducting Quantum Interference Device (SQUID)	62
3.4.1 Introduction	62
3.4.2 Basic Principle and Instrumentation	62
3.5 Raman Spectroscopy	64
3.5.1 Introduction	64
3.5.2 Basic Working	65
3.5.3 Instrumentation	66
3.6 Electrical Measurements	67
3.6.1 Introduction	67
3.6.2 Basic working and Instrumentation	68
3.7 References	70
CHAPTER 4: RESULTS AND DISCUSSIONS	72
4.1 X-Ray Diffraction Analysis	72
4.2 Scanning Electron Microscope Analysis	76
4.3 UV-Visible Diffusive Reflectance Spectroscopy Analysis	80
4.4 The Superconducting Quantum Interference Device (SQUID) Analysis	83
4.5 Raman Spectroscopy Analysis	85
4.6 Electrical Analysis by Network Analyser	88
4.6.1 Variation of Dielectric constant with Frequency	88
4.6.2 Variation of Dielectric loss with Frequency	90
4.6.3 Nyquist's Plots	92
4.7 References	94
CHAPTER 5: CONCLUSION	100

LIST OF ILLUSTRATIONS

Figure 1.1: B-H curve for ferrites (a) soft ferrites and (b) hard ferrites	10
Figure 1.1: Unit cell of (AB ₂ O ₄) spinel	12
Figure 1.3: Schematic of a representative spinel ferrites structure, showing oxygen atoms (red), tetrahedral (yellow), octahedral (green) units. The structure was drawn using the VESTA software.	12
Figure 1.4: Schematic representation of a) Normal-Spinel, b) Mixed-Spinel c) Inverse-Spinel	13
Figure 1.5: GO chemical structure based on the Lerf-Klinowski model.	14
Figure 2.1: Synthesis of spinel ferrite nanoparticles by co-precipitation method.	31
Figure 2.2: Schematic diagram of Spray Pyrolysis Method	32
Figure 2.3: Schematic diagram of Sol-Gel Method	34
Figure 2.4: High Energy Ball Milling Method	35
Figure 2.5: Schematic diagram of Combustion method	37
Figure 2.6: Flow chart of Hydrothermal method	40
Figure 2.7: Schematic diagram of Hofmann's method	41
Figure 2.8: Schematic diagram of Staudenmaier's method	42
Figure 2.9: Schematic diagram of Tour's method	43
Figure 2.10: Flow chart of modified Hummer's method	45
Figure 2.11: Flow chart of Hydrothermal method to prepare ZnFe ₂ O ₄ -GO nanocomposites	47
Figure 2.12: Glimpses of Graphene Oxide preparation process	47
Figure 2.13: Glimpses of Graphene Oxide/Zinc Ferrite preparation process	48
Figure 3.1: X-Ray Diffractometer	52
Figure 3.2: Bragg's Law	53

Figure 3.3: A beam of X-rays directed at a crystal forming a cone	53
Figure 3.4: Three major components of the instrument for powder X-Ray diffraction: 1) X-ray source 2) sample holder; and 3) detector	54
Figure 3.5: Carl Zeiss Scanning Electron Microscope Setup	55
Figure 3.6: Schematic Diagram of SEM	56
Figure 3.7: UV-Visible Spectrometer	58
Figure 3.8: Schematic diagram of UV-Vis Spectrometer	59
Figure 3.9: Two parallel Josephson junction in SQUID	62
Figure 3.10: Principle of a SQUID	63
Figure 3.11: SQUID	63
Figure 3.12: Raman Spectrometer	64
Figure 3.13: Raman scattering	66
Figure 3.14: Working of Raman Spectroscopy	66
Figure 3.15: Block Diagram of Network Analyser	69
Figure 3.16: Electrical Network Analyser	69
Figure 4.1: Rigaku X-ray Diffractometer	72
Figure 4.2 (a): X-Ray Diffraction pattern of GO	73
Figure 4.2 (b): X-Ray Diffraction pattern of ZnFe_2O_4	73
Figure 4.2 (c): X-Ray Diffraction pattern of ZnFe_2O_4	73
Figure 4.2(d): X-Ray Diffraction pattern of $\text{ZnFe}_2\text{O}_4/\text{GO}$ (2.6%)	73
Figure 4.2(e): X-Ray Diffraction pattern of $\text{ZnFe}_2\text{O}_4/\text{GO}$ (3.6%)	73
Figure 4.3: Lattice constant as a function of GO concentration	75
Figure 4.4: Crystallite Size 't' as a function of GO concentration	76
Figure 4.5 Carl Zeiss Scanning Electron Microscope Setup	76
Figure 4.6 (a): SEM image and histogram of ZnFe_2O_4	79

Figure 4.6 (b): SEM image and histogram of ZnFe ₂ O ₄ /GO (1.6%)	79
Figure 4.6 (c): SEM image and histogram of ZnFe ₂ O ₄ /GO (2.5%)	79
Figure 4.6 (d): SEM image and histogram of ZnFe ₂ O ₄ /GO (3.6%)	79
Figure 4.7 UV-Visible Spectroscope	80
Figure 4.8(a): ZnFe ₂ O ₄	82
Figure 4.8(b): ZnFe ₂ O ₄ /GO (1.6%)	82
Figure 4.8(c): ZnFe ₂ O ₄ /GO (2.5%)	82
Figure 4.8(d): ZnFe ₂ O ₄ /GO (3.6%)	82
Figure 4.8 (e): ZnFe ₂ O ₄ and all the composites	82
Figure 4.9: Superconducting Quantum Interference Device (SQUID)	83
Figure 4.10 (a): ZnFe ₂ O ₄	84
Figure 4.10 (b): ZnFe ₂ O ₄ /GO(1.6%)	84
Figure 4.10 (c): ZnFe ₂ O ₄ /GO(2.5%)	84
Figure 4.10 (d): ZnFe ₂ O ₄ /GO(3.6%)	84
Figure 4.11: LabRAM HR Evolution Raman Microscope	85
Figure 4.12: GO, ZnFe ₂ O ₄ and all composites	87
Figure 4.12 (a): ZnFe ₂ O ₄	87
Figure 4.12 (b): ZnFe ₂ O ₄ /GO(1.6%)	87
Figure 4.12 (c): ZnFe ₂ O ₄ /GO(2.5%)	87
Figure 4.12(d) ZnFe ₂ O ₄ /GO(1.6%)	87
Figure 4.13: Network Analyser Set-up	88
Figure 4.14 (a): ZnFe ₂ O ₄	89
Figure 4.14 (b): ZnFe ₂ O ₄ /GO(1.6%)	89
Figure 4.14 (c): ZnFe ₂ O ₄ /GO(2.5%)	89
Figure 4.14 (d): ZnFe ₂ O ₄ /GO(3.6%)	89

Figure 4.14 (e): ZnFe ₂ O ₄ and the as prepared composites	89
Figure 4.15 (a): ZnFe ₂ O ₄	91
Figure 4.15 (b): ZnFe ₂ O ₄ /GO(1.6%)	91
Figure 4.15 (c): ZnFe ₂ O ₄ /GO(2.5%)	91
Figure 4.15 (d): ZnFe ₂ O ₄ /GO(3.6%)	91
Figure 4.15 (e): ZnFe ₂ O ₄ and its composites	91
Figure 4.16(a): ZnFe ₂ O ₄	93
Figure 4.16(b): ZnFe ₂ O ₄ /GO(1.6%)	93
Figure 4.16(c): ZnFe ₂ O ₄ /GO(2.5%)	93
Figure 4.16(d): ZnFe ₂ O ₄ /GO(3.6%)	93

ABSTRACT

The present investigation is focused on structural, morphological, electrical, optical and magnetic properties of novel graphene oxide/ zinc ferrite (GO/ZnFe₂O₄) nanocomposite materials. The graphene oxide (GO) was synthesized using modified Hummer's method and was used during hydrothermal synthesis of ZnFe₂O₄ to obtain GO/ZnFe₂O₄ nanocomposite with three different concentrations of GO (1.6%, 2.5% and 3.6%). The GO/ZnFe₂O₄ nanocomposites were characterized using X-ray diffraction (XRD) for structural confirmation. The morphological study was examined using scanning electron microscope. The optical character of these nanocomposites was investigated using micro-Raman spectroscopy and UV-visible diffusive reflectance spectroscopy. The energy band gap 'E_g' of the nanocomposites was found to decrease with increasing Go concentration in the nanocomposite. The magnetic properties of GO/ZnFe₂O₄ nanocomposites were analyzed using Superconducting Quantum Interference Device (SQUID). The Network analyzer was used to probe the variation of several electrical parameters such as impedance 'Z', dielectric constant 'K' and dielectric loss (Tan δ) due to GO loading on Zinc ferrite. The results obtained on GO/ZnFe₂O₄ nanocomposites demonstrated that these nanocomposites can potentially be used in the field of supercapacitors as electrode material.

CHAPTER 1: INTRODUCTION

1.1 Energy Storage Systems

The modern day energy revolution to put in place a sustainable energy system and solve the energy and environmental crisis, which is caused by the utilization of fossil fuels, is taking place with electricity as its central form of energy. The development, utilization, and storage of large-scale renewable energy are the key elements of the modern-day energy revolution to create a sustainable energy system and address the energy and environmental crisis caused by the use of fossil fuels. The prospect of energy storage applications has risen to prominence with the evolution of grid systems and the support of government policies and investment. The research and demonstration of energy storage technology has grown from small-scale to large-scale because of the swift development of energy storage technology. The outcome of this development will significantly contribute to the design of future power system models.

1.1.1 Classification of energy storage

There are five ways to categorize energy storage technologies based on the type of energy it is stored as, viz, mechanical, heat, electrochemical, magnetic, and chemical energy storage.

A) Mechanical energy storage

The storage of mechanical energy involves applying force to an appropriate medium to generate acceleration, compression, or displacement against gravity, and then the stored kinetic or potential energy can be recovered by reversing the process. The three main technologies for mechanical energy storage are pumped storage, compressed-air energy storage, and flywheel energy storage.

Among these technologies, pumped storage has been most widely developed due to its large capacity, long service lifespan, and low unit cost. However, it is limited by geographical conditions, long construction periods, and high costs. Compressed-air energy storage has advantages such as large capacity, long operation time, and the ability to supply combined heat, cold, and electricity by converting compressed air into alternative energy sources. However, it is a complex system with low efficiency, and requires a high location requirement for the air storage mine tunnel. ^[13]

Flywheel energy storage has several advantages, such as high efficiency, fast response, long service lifespan, minimum operating demands and maintenance, good stability, short construction periods, small footprint, and no pollution. However, it is only suitable for short-duration applications due to its low energy density and tendency for self-discharge. ^[2]

B) Heat storage

Heat storage technology refers to the process of transferring and storing heat energy for later use. There are two main categories of heat storage technology: sensible heat storage and latent heat storage.

Sensible heat storage involves using water as a heat storage medium and increasing the temperature of the storage material to achieve heat storage. Latent heat storage achieves phase change heat storage by using a regenerative material medium, which is commonly used in solar thermal power generation.

Heat storage systems have high energy storage efficiency, reaching up to 95%-97% ^[21], and their cost is only about 1/30 of that of large-scale battery storage systems. Molten salt storage technology has attracted significant interest due to its low cost, high heat capacity, and safety features, making it a potential option for use in solar

thermal power plants. However, there are several practical implementation challenges, including the corrosive nature of the technology being a major drawback.

C) Electrochemical energy storage

Electrochemical energy technology involves the conversion of chemical energy into electrical energy or vice versa. The main examples of electrochemical energy storage technologies include lead-acid batteries, lithium-ion batteries, sodium-sulfur batteries, and redox flow batteries.

Lead-acid batteries are advantageous due to their low cost and easy maintenance, but they also have some drawbacks such as low energy density, shorter life expectancy, and environmental pollution. ^[9] This is because the capacity of the battery decreases under deep, fast, and high power discharge.

Lithium-ion batteries are widely used in various applications, from small electronic devices like smartphones and computers to vehicles. They have many advantages over other batteries, such as a low self-discharge rate, low maintenance, and higher cell voltages. However, they also require a protection/battery management system as they are not very robust, and they have some limitations, such as ageing, transportation restrictions, and cost. Lithium batteries also include lithium iron phosphate, lithium titanate, and nickel-cobalt-manganese lithium batteries.

Redox flow batteries mainly consist of vanadium redox flow batteries and zinc-bromine flow batteries. Vanadium redox flow batteries have a long lifespan and high life cycle, but they also have some drawbacks such as low energy and power density and slow response. Zinc-bromine batteries have a high energy density, low cost, and frequent deep discharge, but they suffer from a high self-discharge rate due to electrode reaction producing a complex.

Sodium-sulphur batteries have a high energy density, good power characteristics, and long cycle life. However, the use of sodium, which is a flammable metal, and the operation at high temperatures (300-350°C) pose safety risks.

D) Electromagnetic energy storage

Electromagnetic energy can be stored as an electric field or magnetic field. Electromagnetic energy storage primarily comprises supercapacitors and superconducting magnetic energy storage. Supercapacitors have many advantages such as high power density, fast response, high efficiency, long cycle life, low maintenance, and a wide operational temperature range. However, due to their low energy density, they are better suited for use in conjunction with other energy storage technologies. ^[25] The critical parameter for superconducting magnetic energy storage is its charging/discharging rate. It is typically used in high-power applications because it has high power density, fast response, high energy conversion efficiency, and a long service life. Nevertheless, it is associated with some drawbacks, such as high cost, low energy density, and complicated maintenance. ^[11]

E) Chemical energy storage.

Chemical energy storage is the storage of energy in the form of chemical fuels that can be easily converted to other forms of energy. Hydrogen and synthetic gas are considered as secondary energy carriers, with hydrogen being produced through electrolysis and can be synthesized into natural gas when combined with carbon dioxide. This is a clean technology that does not cause pollution, and it has the potential to create large-scale energy storage systems that can store over 100 GWh of energy. However, due to its low energy conversion efficiency of only 40%-50%, high cost, large initial investment, and low security, there are several challenges to its practical application. ^[7]

1.1.2 Emerging technologies

With the rapid development of material science, researches on new energy storage technologies such as graphene based energy storage technologies are also carried out.

1.2 Nanomaterials, Nanoparticles, Nanotechnology and Nanocomposites

Nanomaterials have become widely recognized due to their diverse range of applications. The European Commission has defined nanomaterials as natural, accidental, or synthetic materials composed of particles that are either unattached or clustered together with at least one external dimension in the 1-100 nm range, making up more than half of the particles based on number size distribution. ^[18]

The utilization of nanomaterials in the production of the active electrode of supercapacitors has enhanced the performance of electric double-layer capacitors, pseudo-capacitors, and hybrid capacitors. The progress in research and development of nanomaterials has resulted in significant improvements in the performance of supercapacitors. ^[19]

While nanomaterials are materials with any internal or external structures on the nanoscale dimensions, Nanoparticles are Nano-object (Materials that possesses one or more peripheral nanoscale dimensions.) with three external nanoscale dimensions. ^[8]

Magnetic metal oxide nanoparticles have become a desirable option for inorganic solids as they are low-cost and can be produced in large quantities with ease.

Spinel ferrites and inorganic perovskite oxides are among the superior magnetic materials for serving as electrodes in supercapacitor applications. Research has shown that spinel ferrites, composed of various elements, can be used to design supercapacitor energy storage devices. These nanomaterials have a high energy density, durability, good capacitance retention, high power, and long-term stability. ^[5]

Spinel ferrites do have some limitations due to its high density. These shortcomings can be constrained by the addition of graphene oxide (GO).^[6] Graphene and its oxide have low density, high specific surface area, and mechanical strength.^[17] So, the permeability of ferrite can be integrated with higher dielectric loss and electrical conductivity of graphene oxide.

A composite material is produced by combining two or more materials with different physical or chemical properties to form a new material with unique properties. Nanocomposites are created by combining materials at the nanoscale level. This technology utilizes the best features of different elements to create a highly efficient material. The combination of spinel ferrites and graphene in nanocomposites can lead to the attainment of various properties such as increased specific surface area, higher power density, controllable pore size, enhanced electrical conductivity, and more.^[15]

1.3 Nanocomposites in energy storage applications

Nanocomposites have been extensively researched for their potential use in energy storage applications. The high surface area and unique properties of nanoparticles allow for improved performance in a range of energy storage systems such as batteries, supercapacitors, and fuel cells.

In particular, nanocomposites show promise in improving the capacity, rate capability, and cycling stability of lithium-ion batteries (LIBs). For example, the incorporation of graphene oxide (GO) into zinc ferrite (ZnFe_2O_4) nanocomposites has been shown to enhance the electrochemical performance of LIB anodes, with improved capacity and cycling stability. Similarly, the use of metal oxide nanoparticles such as TiO_2 , ZnO , and Fe_3O_4 in nanocomposites with carbonaceous materials has also been shown to improve the performance of LIBs.^[22]

In addition, nanocomposites have also been investigated for use in supercapacitors, with studies showing improved specific capacitance and cycling stability when using carbon nanotube (CNT) or graphene-based nanocomposites. Moreover, the use of nanocomposites in fuel cells has shown potential in improving the catalytic activity of electrodes, leading to enhanced power density and durability.

Overall, the incorporation of nanoparticles in nanocomposites has shown promise in improving the performance of energy storage systems. Further research is needed to optimize the synthesis and design of nanocomposites for specific applications.

1.4 Ferrites in energy storage application

Ferrites have gained significant attention in energy storage applications due to their unique magnetic and electrical properties. Among the various types of ferrites, zinc ferrite has emerged as a promising material for energy storage devices, such as lithium-ion batteries (LIBs) and supercapacitors. Zinc ferrite offers several advantages, such as high specific capacity, good structural stability, and low cost, making it an attractive candidate for LIB anodes.

Recently, the combination of zinc ferrite with graphene oxide (GO) has been investigated to further enhance its electrochemical performance. GO offers excellent electrical conductivity and a high surface area, which can improve the electrical conductivity of the active material and increase the access of the electrolyte to the material surface. Moreover, the unique properties of GO, such as its rich oxygen and defect framework, enable it to form nanocomposites with zinc ferrite and other materials.

Several studies have demonstrated the potential of zinc ferrite GO nanocomposites in energy storage applications. For instance, Liu et al. synthesized a zinc ferrite GO

nanocomposite and found that it exhibited improved electrochemical performance, such as higher specific capacity and better cycling stability, compared to pure zinc ferrite. Similarly, Zhang et al. reported that a zinc ferrite GO nanocomposite exhibited excellent rate capability and cycling stability as an anode material for LIBs. ^[14]

In conclusion, zinc ferrite GO nanocomposites have shown great potential in energy storage applications. Further studies are needed to optimize the synthesis and improve the electrochemical performance of these materials.

1.5 Ferrites

Ferrites, which are ceramic oxides with Fe₂O₃ as their main constituent, exhibit both magnetic and electrical properties, making them a type of magnetic material. Due to their ionic nature, ferrites have low eddy current, high electrical resistivity, and dielectric losses, making them ideal for use in various technological applications. ^[10]

1.5.1 Classification of ferrites

Ferrites are ionic compounds that consist of double oxides of iron and other metals, and their magnetic properties are determined by the type of ions they contain. Some ferrites occur naturally as impurities in rocks, and they typically have a dark grey or black color and a hard, brittle ceramic texture. Ferrites can be produced by heating transition metal oxides ^[1], and they can be classified based on their magnetic characteristics and crystal structure.

According to magnetic properties

Ferrites can be classified into two groups based on their magnetic properties: soft ferrites and hard ferrites. Soft ferrites exhibit low coercivity of magnetism, as shown in the figure, while hard ferrites exhibit high coercivity of magnetism, as also shown in the figure. ^[1]

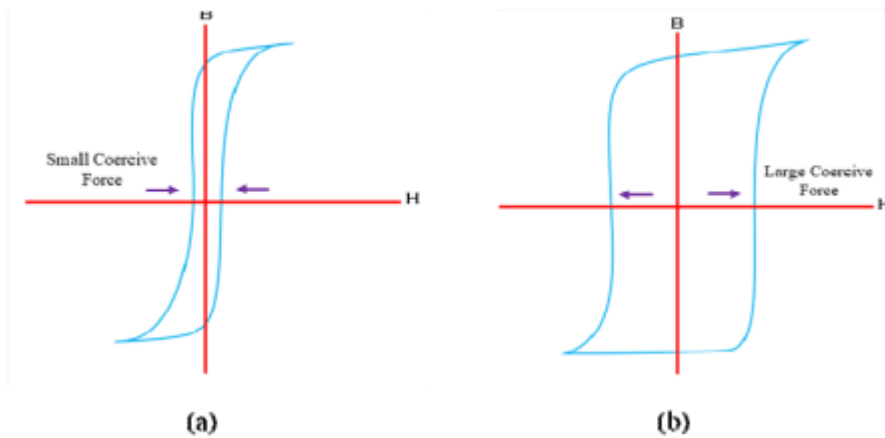


Figure 2.1: B-H curve for ferrites (a) soft ferrites and (b) hard ferrites.^[1]

Soft Ferrites

Soft ferrites refer to ferrimagnetic materials that lose their magnetism after being magnetized. They possess a magnetization curve that rises steeply, a small and narrow hysteresis loop, and minimal energy losses during magnetization. These materials are produced through the process of heating and slow cooling, and they can be easily magnetized and demagnetized. Soft ferrites are ceramic insulators with a cubic crystal structure of MFe_2O_4 , where M denotes transition metal ions such as Ni, Mn, and Zn. They have high susceptibility and permeability values, low eddy current losses, and low retentivity and coercivity. As a result, soft ferrites are used in various applications, including electromagnets, computer data storage, transformer cores, telephone signal transmitters and receivers, and more. ^[1]

Hard Ferrites

Hard ferrites are referred to as permanent magnetic materials due to their ability to retain their magnetism even after being magnetized. These ferrimagnetic materials have a gradually increasing magnetization curve, a large hysteresis loop, and high energy losses during magnetization. Hard ferrites are created by heating and then rapidly cooling the material, and they are not easily magnetized or demagnetized.

They are made up of iron and either barium or strontium oxides. Hard ferrites have high saturation flux density, low susceptibility and permeability, high eddy current losses, and high retentivity and coercivity. These properties make them ideal for use in permanent magnets, DC magnets, loudspeakers, and other applications. [1]

According to Crystal Structure

Ferrites exhibit a range of crystal structures and can be classified into four different types based on these structures. These four types include spinel, garnet, ortho, and hexagonal ferrites.

Sr. No.	Types	Molar ratio	Representation
1	Spinel	$Fe_2O_3 \cdot MO$	MO is a transition metal oxide
2	Garnet	$5Fe_2O_3 \cdot 3M_2O_3$	M_2O_3
3	Ortho	$AFeO_3$	A is rare earth elements (Ho, Dy, Er, Y, Yb, etc)
4	Hexagonal	$6Fe_2O_3 \cdot MO$	MO is a divalent metal oxide from group IIA (BaO, CaO, SrO, etc)

1.6 Spinel Oxides

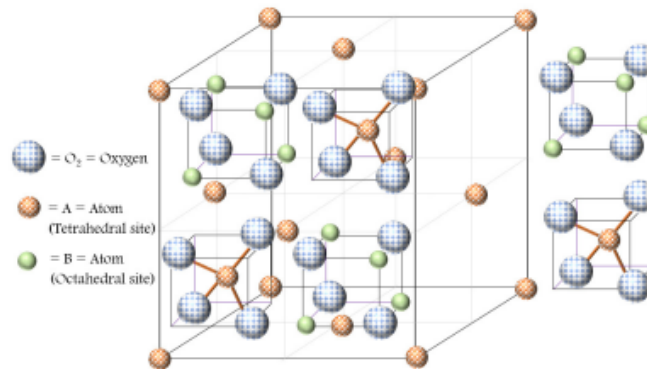


Figure 1.3: Unit cell of (AB₂O₄) spinel ^[1]

Spinel-type oxides are a group of materials that have a face-centered cubic (FCC) crystal structure with a general formula of AB₂O₄. Typically, A and B represent divalent and trivalent cations, respectively. When these systems contain iron as the main component, they are referred to as spinel ferrites.

1.7 Spinel Ferrites

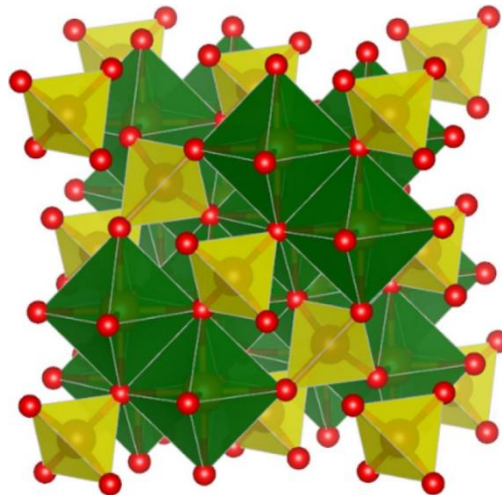


Figure 1.4: Schematic of a representative spinel ferrite structure, showing oxygen atoms (red), tetrahedral (yellow), octahedral (green) units. The structure was drawn using the VESTA software. ^[3]

A spinel ferrite is a type of complex oxide crystal structure that has a face-centered cubic core and a unit formula of AFe_2O_4 . It can be created by combining a trivalent cation (Fe^{3+}) with a divalent metallic cation, such as a transition or post-transition metallic cation ($A = Mn, Mg, Co, Ni, Zn$). The cations can be arranged into two crystallographic sites, tetrahedral and octahedral, based on their chemical nature, charge state, and stabilization energy. The AFe_2O_4 unit has 32 oxygen atoms, 64 divalent tetrahedral sites, and 32 trivalent octahedral sites, with A^{2+} and Fe^{3+} usually occupying 8 tetrahedral and 16 octahedral sites, respectively, to maintain an electrically balanced state. The spinel ferrite structure can be classified as normal, inverse, or mixed based on the positions of these cations, which depend on factors such as electrostatic contribution to the lattice energy, cation radii, cation charges, and crystal field effects.

In a typical spinel ferrite structure, the A^{2+} cations are found at tetrahedral sites, while Fe^{3+} cations are located at octahedral sites, as seen in structures like $ZnFe_2O_4$, $CoAl_2O_4$, $MgAl_2O_4$, and Mn_3O_4 . In the inverse spinel structure, Fe^{3+} cations are distributed equally between tetrahedral and octahedral sites, while A^{2+} cations only occupy octahedral sites, as in $NiFe_2O_4$, $CoFe_2O_4$, Fe_3O_4 , and others. In a mixed spinel structure, A^{2+} and Fe^{3+} cations randomly occupy both sites, as seen in structures like $MgFe_2O_4$ and $MnFe_2O_4$.^[16]

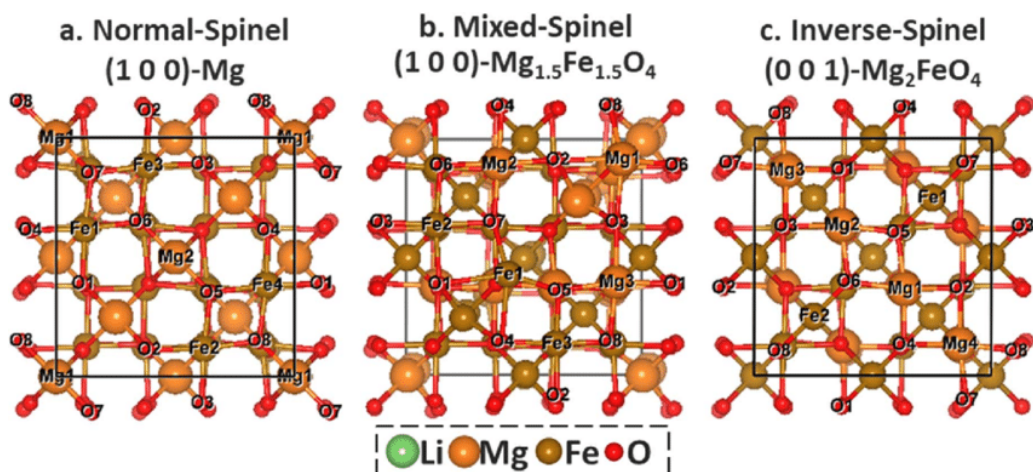


Figure 1.5: Schematic representation of a) Normal-Spinel, b) Mixed-Spinel c)
Inverse-Spinel ^[26]

The magnetic, electrical, microwave absorption, and photocatalytic properties of zinc ferrite have made it a subject of extensive research in recent years. ^[13]

1.8 Zinc Ferrite

Zinc ferrite has gained attention due to its unique properties, such as magnetic, electrical, microwave absorption, and photocatalytic properties. Its structure follows a traditional normal spinel ferrite, where Zn^{2+} ions occupy tetrahedral A-sites and Fe^{3+} ions occupy octahedral B-sites. In this structure, the magnetic moment is equal and arranged in opposite directions, resulting in no magnetism displayed. However, at higher temperatures, partial occupation of Zn^{2+} ions in B-sites creates an intermediate spinel ferrite, exhibiting ferrimagnetism.

Recent advancements in synthetic methods and material combinations have enabled the production of controllable morphology and structure of zinc ferrite, improving its applications. Zinc ferrite ($ZnFe_2O_4$) is being explored as a potential candidate for LIB anodes due to its non-toxicity, environmental friendliness, structural stability, and low cost. However, its low rate capability and poor cycling performance caused by electrode pulverization during lithiation/delithiation processes limit its potential. ^[13] To mitigate these issues, researchers have turned to using graphene, a two-dimensional carbon nanomaterial with excellent conductivity and flexibility, as a carbonaceous material to improve the cycling stability of LIB electrodes. ^[23]

1.9 Graphene Oxide

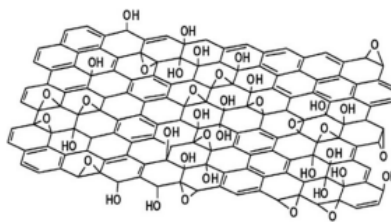


Figure 1.6: GO chemical structure based on the Lerf-Klinowski model. [6]

The layered structure of graphite oxide is similar to that of graphite. However, the plane of carbon atoms in graphite oxide is adorned with oxygen-containing groups. These groups increase the distance between layers and make them hydrophilic. When these oxidized layers are subjected to ultrasonication in water, they can be exfoliated. If these exfoliated sheets have only one or a few layers of carbon atoms like graphene, they are referred to as graphene oxide (GO). GO is a single-layered material made by oxidizing graphite crystals that contain carbon, hydrogen, and oxygen molecules. Graphite crystals are abundant and inexpensive. GO is easily processed and dispersible in water. [4]

1.10 Aim of Present study

The expectation is that when ZnFe_2O_4 is combined with conductive graphene nanosheets, the resulting material would have improved electrochemical performance. This is because the combination would increase the electrical conductivity of the active material and allow better access of the electrolyte to the material surface. [4]

GO possesses outstanding electrical, mechanical, and electrochemical characteristics. In addition, its high surface area and abundant oxygen and defect framework make it a suitable candidate for forming nanocomposites with metal/semiconductor nanoparticles, metal oxides, quantum dots, and polymers. These nanocomposites are gaining importance in various industries. [20]

The prime objective of the present study is to synthesize Zinc Ferrite Graphene Oxide nanocomposites at varying concentrations of Graphene Oxide composition in Zinc

Ferrite and to study its structural, morphological, electrical and magnetic properties of the synthesised novel graphene oxide/ zinc ferrite (GO/ZnFe₂O₄).

1.11 Literature Review

Rizwan Ali et al. synthesized GO/ZnFe₂O₄ nanocomposite via a hydrothermal method, and its morphological, structural, and magnetic properties were characterized using various techniques, including X-ray diffraction (XRD), scanning electron microscopy (SEM), transmission electron microscopy (TEM), Fourier transform infrared (FTIR) spectroscopy, UV-vis spectroscopy, and vibrating sample magnetometry (VSM). The DOX-loaded GO/ZnFe₂O₄ nanocomposite was prepared via a simple adsorption method, and its drug loading and release properties were evaluated. The cytotoxicity and cellular uptake of the nanocomposite were investigated in vitro using human breast cancer cells (MCF-7), and its MRI contrast enhancement ability was evaluated using a 1.5 T clinical MRI scanner. The results indicated that the GO/ZnFe₂O₄ nanocomposite had a uniform distribution of ZnFe₂O₄ nanoparticles on the surface of the GO sheets. The SEM and TEM images revealed that the average particle size of the ZnFe₂O₄ nanoparticles was around 40 nm. The FTIR spectra confirmed the presence of ZnFe₂O₄ and GO in the nanocomposite. The VSM measurements showed that the nanocomposite had superparamagnetic behavior with a high saturation magnetization value. The DOX loading and release studies demonstrated that the nanocomposite had a high drug loading capacity and sustained drug release behavior. The in vitro cytotoxicity studies showed that the DOX-loaded GO/ZnFe₂O₄ nanocomposite had a higher anti-cancer activity than free DOX due to the synergistic effect between the nanocomposite and the drug. The cellular uptake studies revealed

that the nanocomposite had efficient cellular internalization in MCF-7 cells. The MRI studies showed that the nanocomposite had a high contrast enhancement effect, indicating its potential as an MRI contrast agent. In conclusion, the results of this study demonstrate the potential of the GO/ZnFe₂O₄ nanocomposite loaded with DOX as a theranostic medium for cancer therapy and MRI. The nanocomposite has several advantages, including high drug loading capacity, sustained drug release behavior, efficient cellular internalization, and high MRI contrast enhancement effect. The hydrothermal method used in this study provides a simple and scalable approach for the synthesis of the nanocomposite. Further research is needed to optimize the properties and performance of the nanocomposite and to explore its potential for other biomedical applications.

S.Sadighian et al. synthesized ZnFe₂O₄-GO nanocomposite using a co-precipitation method, and its morphological, structural, and magnetic properties were characterized using various techniques, including X-ray diffraction (XRD), scanning electron microscopy (SEM), transmission electron microscopy (TEM), Fourier transform infrared (FTIR) spectroscopy, and vibrating sample magnetometry (VSM). The dye adsorption experiments were conducted using two different dyes, Methylene Blue (MB) and Rhodamine B (RhB), and the effect of various parameters, such as pH, initial dye concentration, contact time, and temperature, were investigated. The results indicated that the ZnFe₂O₄-GO nanocomposite had a uniform distribution of ZnFe₂O₄ nanoparticles on the surface of the GO sheets. The SEM and TEM images revealed that the average particle size of the ZnFe₂O₄ nanoparticles was around 30 nm. The FTIR spectra confirmed the presence of ZnFe₂O₄ and GO in the nanocomposite. The VSM measurements showed that the nanocomposite had superparamagnetic behavior

with a high saturation magnetization value. The dye adsorption experiments showed that the ZnFe_2O_4 -GO nanocomposite had a high adsorption capacity for both MB and RhB, with the maximum adsorption capacity of 131.58 mg/g for MB and 103.09 mg/g for RhB. The adsorption process was found to be pH-dependent, with the optimum pH for dye removal being 7. The adsorption kinetics and isotherms were analyzed, and it was found that the adsorption process followed a pseudo-second-order kinetic model and Langmuir isotherm model, respectively. The thermodynamic parameters indicated that the adsorption process was spontaneous and exothermic. In conclusion, the results of this study demonstrate the potential of the ZnFe_2O_4 -GO nanocomposite for the removal of dye from water. The nanocomposite has several advantages, including a high adsorption capacity, magnetic separability, and easy regeneration. The co-precipitation method used in this study provides a simple and cost-effective approach for the synthesis of the nanocomposite. Further research is needed to optimize the properties and performance of the nanocomposite and to explore its potential for other environmental applications.

Rajarshi Bhattacharyya et al., synthesized graphene oxide-ferrite hybrid framework using a hydrothermal method, and its morphological, structural, and microwave absorption properties were characterized using various techniques, including X-ray diffraction (XRD), Fourier transform infrared (FTIR) spectroscopy, Raman spectroscopy, scanning electron microscopy (SEM), and vector network analyzer (VNA) measurements. The microwave absorption properties were evaluated using the reflection loss (RL) method, and the effect of various parameters, such as filler content, thickness, and frequency, were investigated. The results indicated that the graphene oxide-ferrite hybrid framework had a unique 3D interconnected porous

structure, which provided a large surface area for electromagnetic wave absorption. The SEM images revealed that the framework had a uniform distribution of graphene oxide and ferrite particles. The FTIR and Raman spectra confirmed the presence of graphene oxide and ferrite in the hybrid framework. The VNA measurements showed that the hybrid framework had a broad absorption bandwidth of more than 4 GHz and a maximum reflection loss of -50 dB at a frequency of 10 GHz. The effect of filler content and thickness on the absorption properties was also investigated, and it was found that the optimum filler content and thickness for maximum absorption were 30 wt% and 2.5 mm, respectively. The microwave absorption mechanism was analyzed, and it was found that the enhanced absorption was due to the combined effect of dielectric loss, magnetic loss, and multiple reflection losses within the porous structure of the hybrid framework. In conclusion, the results of this study demonstrate the potential of the graphene oxide-ferrite hybrid framework for enhanced broadband absorption in gigahertz frequencies. The hybrid framework has several advantages, including a large surface area, uniform distribution of particles, and enhanced absorption properties. The hydrothermal method used in this study provides a simple and scalable approach for the synthesis of the hybrid framework. Further research is needed to optimize the properties and performance of the hybrid framework and to explore its potential for practical applications in various fields.

Yuheng Tian et al. first discussed the various methods for the synthesis of graphene oxide, including the Hummers' method, the Staudenmaier method, and the improved Hummers' method. They then highlighted the unique properties of graphene oxide, such as its high specific surface area, tunable electronic properties, and strong adsorption capability. The electronic properties of graphene oxide can be tuned by

controlling the degree of oxidation and functionalization of the graphene sheets. The strong adsorption capability of graphene oxide makes it a suitable material for energy storage and conversion applications. Tian and colleagues then discussed the various applications of graphene oxide in energy storage, such as in supercapacitors and batteries. Graphene oxide has been used as an electrode material in supercapacitors due to its high surface area and electrical conductivity. The authors highlighted the recent advancements in the development of graphene oxide-based electrodes with enhanced capacitance and stability. Graphene oxide has also been used as a conductive additive in lithium-ion batteries to improve their performance. The authors then discussed the various applications of graphene oxide in energy conversion, such as in fuel cells and solar cells. Graphene oxide has been used as a catalyst support in fuel cells due to its high surface area and stability. The authors highlighted the recent advancements in the development of graphene oxide-based catalysts with enhanced catalytic activity and durability. Graphene oxide has also been used as a transparent conductive electrode in solar cells to improve their efficiency. In conclusion, the authors provided a comprehensive overview of the recent advances in the synthesis, properties, and applications of graphene oxide in energy storage and conversion. Graphene oxide has emerged as a promising electromaterial due to its unique properties and has shown great potential in various energy-related applications. The authors emphasized the need for further research to optimize the properties and performance of graphene oxide-based materials and to explore their potential for practical applications in the energy sector.

Shyamalee Patar et al. have reported a novel zinc ferrite anchored graphene oxide magnetic nanocomposite for the photocatalytic degradation of textile dyes. The

nanocomposite was synthesized using a simple solvothermal method and characterized using various techniques such as X-ray diffraction, transmission electron microscopy, and Fourier transform infrared spectroscopy. The results showed that the nanocomposite had a unique hierarchical structure with zinc ferrite nanoparticles anchored onto the surface of graphene oxide sheets. The photocatalytic activity of the nanocomposite was evaluated by the degradation of two different dyes, namely, methylene blue and rhodamine B. The results showed that the nanocomposite exhibited excellent photocatalytic activity, with degradation rates of 99% and 95% for methylene blue and rhodamine B, respectively, within 90 minutes of irradiation under visible light. In conclusion, the synthesis of the novel zinc ferrite anchored graphene oxide magnetic nanocomposite reported by Shyamalee Patar et al. has shown promising results for the photocatalytic degradation of textile dyes. The incorporation of magnetic materials into graphene oxide-based photocatalysts can greatly enhance their separation efficiency and recycling potential, making them highly attractive for practical applications.

Qin et al. synthesized the zinc ferrite composite material by mixing zinc nitrate hexahydrate, iron nitrate nonahydrate, and sodium hydroxide in ethylene glycol and water solvent, followed by heating the mixture in a sealed Teflon-lined autoclave at 180°C for 12 hours. By varying the ratio of the precursors, the authors were able to control the morphology of the zinc ferrite particles, producing either cubic or octahedral-shaped particles. The study further demonstrated the potential applications of the zinc ferrite composite material by using it as a catalyst for the degradation of Rhodamine B dye under visible light irradiation. The results showed that the composite material exhibited excellent photocatalytic activity, with more than 95% of

the dye being degraded within 120 minutes. The study by Qin et al. provides a novel and facile approach for synthesizing zinc ferrite composite materials with controllable morphology and demonstrates their potential applications in photocatalysis. This research provides valuable insights for further developing and optimizing zinc ferrite-based materials for various applications.

Kooti et al. synthesized the nanocomposite using in-situ chemical oxidative polymerization of aniline in the presence of RGO and CoFe_2O_4 . The resulting nanocomposite was characterized using various techniques, including X-ray diffraction (XRD), transmission electron microscopy (TEM), and Fourier transform infrared spectroscopy (FTIR). The results indicated that the nanocomposite exhibited a high degree of crystallinity and the presence of RGO and CoFe_2O_4 resulted in the formation of a porous structure with a high specific surface area. The electromagnetic properties of the nanocomposite were evaluated by measuring its electromagnetic wave absorption properties in the frequency range of 8.2-12.4 GHz. The results showed that the nanocomposite exhibited a high degree of electromagnetic wave absorption, with a maximum absorption of -40 dB at a thickness of 5.5 mm. The authors attributed this high absorption to the synergistic effect of the RGO, PANI, and CoFe_2O_4 , which resulted in a strong interfacial polarization and multiple reflection and absorption of the electromagnetic waves. Overall, the study demonstrated the potential use of the RGO-PANI- CoFe_2O_4 nanocomposite as a promising material for electromagnetic wave absorption applications. The synthesis method used in this study also provides a simple and effective approach for the preparation of ternary nanocomposites with enhanced electromagnetic properties.

Sohail et al. propose a modified and improved Hummer's synthesis method for the preparation of GO for capacitor applications. The modifications to the Hummer's method include the use of a higher concentration of graphite and potassium permanganate, as well as increased reaction time and the addition of a sonication step. The synthesized GO was characterized by various techniques, including Fourier transform infrared spectroscopy (FTIR), Raman spectroscopy, X-ray diffraction (XRD), and scanning electron microscopy (SEM). The results showed that the modified Hummer's method produced GO with a high degree of oxidation, a large surface area, and a high electrical conductivity. The authors then tested the performance of the synthesized GO in a capacitor device and compared it to a commercial capacitor. The results showed that the GO-based capacitor had a higher capacitance and better charge-discharge cycling performance than the commercial capacitor. Overall, this study demonstrates the potential of the modified Hummer's method for the synthesis of GO for use in energy storage applications such as capacitors.

Yao et al. investigates the potential of mesoporous zinc ferrite/graphene composites as a high-performance anode material for lithium-ion batteries. The synthesis of the composite was carried out using a simple and scalable sol-gel method, with zinc nitrate and graphene oxide as the precursors. The results of this study show that the incorporation of graphene into the zinc ferrite structure leads to a significant improvement in the electrochemical performance of the composite. Specifically, the mesoporous zinc ferrite/graphene composite demonstrated a high reversible capacity of 1100 mAh/g at a current density of 100 mA/g, which is much higher than that of pure zinc ferrite (240 mAh/g). The composite also showed excellent rate capability,

with a reversible capacity of 610 mAh/g even at a high current density of 5 A/g. Additionally, the mesoporous structure of the composite was found to enhance its lithium-ion diffusion kinetics, leading to improved cycling stability and a low capacity fading rate. Overall, this study demonstrates the potential of mesoporous zinc ferrite/graphene composites as high-performance anode materials for lithium-ion batteries. The simple and scalable synthesis method and excellent electrochemical properties of this composite make it a promising candidate for use in next-generation energy storage devices.

Sun et al. (2018) summarize recent advancements in the fabrication of printable nanomaterials for supercapacitor electrodes. They highlight the advantages and disadvantages of various nanomaterials, such as graphene oxide, carbon nanotubes, and metal oxides, and their composites. The authors also discuss the fabrication methods, including inkjet printing, screen printing, and spray coating, and their influence on the electrochemical performance of supercapacitor electrodes.

Among the printable nanomaterials, graphene oxide has received significant attention due to its high surface area, good electrical conductivity, and excellent mechanical properties. The authors discuss the preparation of graphene oxide ink, the printing process, and the post-treatment steps to improve the electrical conductivity of the printed graphene oxide films. In addition, the use of graphene oxide composites, such as graphene oxide/carbon nanotubes and graphene oxide/metal oxides, to enhance the electrochemical performance of supercapacitor electrodes is also reviewed.

Overall, the review provides a comprehensive overview of the recent progress in the use of printable nanomaterials for the fabrication of high-performance supercapacitors. The authors highlight the potential of printable nanomaterials to address the challenges associated with conventional supercapacitor electrodes, such as low energy density and poor stability, and suggest directions for future research in this field.

1.12 References

1. Ajitanshu Vedrtam, Kishor Kalauni, Sunil Dubey, Aman Kumar. A comprehensive study on structure, properties, synthesis and characterization of ferrites[J]. *AIMS Materials Science*, 2020, 7(6): 800-835.
2. Chen YA, Gan SL, Zhou JH et al (2016) Energy storage technology of flywheel. *Chin J Power Sour* 40(8):1718–1721
3. D. Harikishore Kumar Reddy, Yeoung-Sang Yun, Spinel ferrite magnetic adsorbents: Alternative future materials for water purification? *Coordination Chemistry Reviews*, Volume315, 2016, Pages 90-111, ISSN 0010-8545.
4. Dideikin Artur T., Vul' Alexander Y., Graphene Oxide and Derivatives: The Place in Graphene Family, *Frontiers in Physics* 6 2019, ISSN 2296-424X.
5. Elkholy, Ayman E. and El-Taib Heakal, F. and Allam, Nageh K. Nanostructured spinel manganese cobalt ferrite for high-performance supercapacitors. *RSC Adv.* 7 (82) 2017, 51888-51895.
6. F Perrozzi and S Prezioso and L Ottaviano, Graphene oxide: from fundamentals to applications, *Journal of Physics: Condensed Matter*, 27(1), 2014, 013002.
7. Huo XX, Wang J, Jiang L et al (2016) Review on key technologies and applications of hydrogen energy storage system. *Energy Storage Sci Technol* 5(2):197–203
8. Jeevanandam, J.; Barhoum, A.; Chan, Y. S.; Dufresne, A.; Danquah, M. K. Beilstein J. *Nanotechnol.* 2018, 9, 1050–1074.
9. Jia LL, Liu P, Zhang WH (2014) Research progress of electrochemical technology of energy storage. *Chin J Power Sour* 40(8):1972–1974
10. Kumar, H., Srivastava, R. C., Negi, P., Agrawal, H. M., & Asokan, K. (2013). Dielectric behaviour of cobalt ferrite nanoparticles. *Int. J. Electr. Electron. Eng*, 2, 59-66.

11. Luo X, Wang J, Dooner M et al (2015) Overview of current development in electrical energy storage technologies and the application potential in power system operation. *Appl Energy* 137:511–536
12. Mei S, Wang J, Tian F et al (2015) Design and engineering implementation of non-supplementary fired compressed air energy storage system: TICC-500. *Sci China Technol Sci* 58(4):600–611
13. Ming Qin, Qin Shuai, Guanglei Wu, Bohan Zheng, Zhengdong Wang, Hongjing Wu, Zinc ferrite composite material with controllable morphology and its applications, *Materials Science and Engineering: B*, Volume 224, 2017, Pages 125-138, ISSN 0921-5107.
14. Mukherjee, S., Saha, S. K., Ghosh, B., & Chakravorty, D. (2018). Zinc ferrite-graphene oxide nanocomposites for high-performance supercapacitor electrode. *Journal of Materials Science: Materials in Electronics*, 29(14), 11902-11911.
15. Najib, Sumaiyah and Erdem, Emre, Current progress achieved in novel materials for supercapacitor electrodes: mini review, *Nanoscale Adv.* 1(8) 2019 2817-2827
16. Pham, Tuyet Nhung and Huy, Tran Quang and Le, Anh-Tuan, Spinel ferrite (AFe₂O₄)-based heterostructured designs for lithium-ion battery, environmental monitoring, and biomedical applications, *RSC Adv.* 10 (52) 2020 31622-31661
17. Senthil Kumar, E., Sivasankar, V., Sureshbabu, R., Raghu, S., A. Kalaivani, R. (2017). Facile synthesis of few layer graphene from bituminous coal and its application towards electrochemical sensing of caffeine. *Advanced Materials Letters*, 8(3), 239-245.
18. Soares Sara, Sousa João, Pais Alberto, Vitorino Carla. *Nanomedicine: Principles, Properties, and Regulatory Issues. Frontiers in Chemistry* 6. ISSN 2296-2646 (2018). 10.3389/fchem.2018.00360

19. Sun, J., Cui, B., Chu, F., Yun, C., He, M., Li, L., & Song, Y. (2018). Printable Nanomaterials for the Fabrication of High-Performance Supercapacitors. *Nanomaterials*, 8(7), 528.
20. Thangamuthu, M., Hsieh, K. Y., Kumar, P. V., & Chen, G. Y. (2019). Graphene- and Graphene Oxide-Based Nanocomposite Platforms for Electrochemical Biosensing Applications. *International journal of molecular sciences*, 20(12), 2975.
21. Vick BD, Moss TA (2013) Adding concentrated solar power plants to wind farms to achieve a good utility electrical load match. *Solar Energy* 92:298–312
22. Wu, Hao Bin and Chen, Jun Song and Hng, Huey Hoon and Wen (David) Lou, Xiong, Nanostructured metal oxide-based materials as advanced anodes for lithium-ion batteries, *Nanoscale*, 2012, volume, 4, issue 8, pages 2526-2542, The Royal Society of Chemistry.
23. Xiayin Yao, Junhua Kong, Dan Zhou, Chenyang Zhao, Rui Zhou, Xuehong Lu, Mesoporous zinc ferrite/graphene composites: Towards ultra-fast and stable anode for lithium-ion batteries, *Carbon*, Volume 79, 2014, Pages 493-499, ISSN 0008-6223.
24. YAO, L., YANG, B., CUI, H. et al. Challenges and progresses of energy storage technology and its application in power systems. *J. Mod. Power Syst. Clean Energy* 4, 519–528 (2016).
25. Zhang XY, Zhang HZ, Lin ZQ et al (2016) Recent advances and challenges of stretchable supercapacitors based on carbon materials. *Sci China Mater* 59(6):475–494
26. Guo, H., Qin, X., Zhang, M., Shi, S., Liu, H., & Zhuang, L. (2020). Essential Role of Spinel MgFe₂O₄ Surfaces during Discharge. *Journal of The Electrochemical Society*, 167(9), 090506

CHAPTER 2: METHODS OF MATERIAL PREPARATION

Nanoparticles have gained significant interest due to their unique chemical and physical properties and are applicable in diverse areas. Various methods of nanoparticles preparation have been developed and they are suitable for synthesis of nanoparticles in different sizes and shapes. The properties of the particles at the nanoscale are greatly influenced by the technique used for its synthesis. The size and shape of the nanoparticles can regulate their physical and chemical properties to a great extent. ^[1] Hence the selection of suitable techniques to obtain the desired nanoparticle becomes essential. Here we have mentioned some of the common and effective methods of preparation of ferrite nanoparticles and graphene oxide nanoparticles with their advantages and disadvantages.

2.1 Methods of preparation of ferrite nanoparticles.

2.1.1 Co-precipitation method

Co-precipitation method is a facile and convenient approach to prepare nanoparticles especially spinel ferrites. This method is as a simple, cost-effective and fast process, easily transposable on a larger scale for industrial applications which also grants a nanomaterial with high purity through an eco-friendly route, without requiring hazardous organic solvents, nor treatments under high pressure or temperature. ^[2] The process involves addition of stoichiometric amounts of desired aqueous metal salt solution with continuous and vigorous stirring in an alkaline solution. The pH of the solution plays important role in the formation of different types of spinel nano ferrites and needs careful monitoring in order to maintain pH

level of 11-12 and achieve high-quality materials. NaOH can be used as a precipitating agent as well as for controlling the pH of the solution depending upon the precursors used. [2,3]

Advantages:

1. It is an eco-friendly route that grants nanomaterial with high purity without requiring hazardous organic solvents.
2. Homogeneous mixing of reacting materials, decrease in the reaction temperature, and formation of uniform-sized nanoparticles.

Disadvantages:

1. Traces of impurities may also get precipitated with the product obtained, it is time consuming.
2. This method does not work well if the reactants have very different precipitation rates.

[4]

Figure 2.1 shows the schematic diagram of experimental setup used in this method.

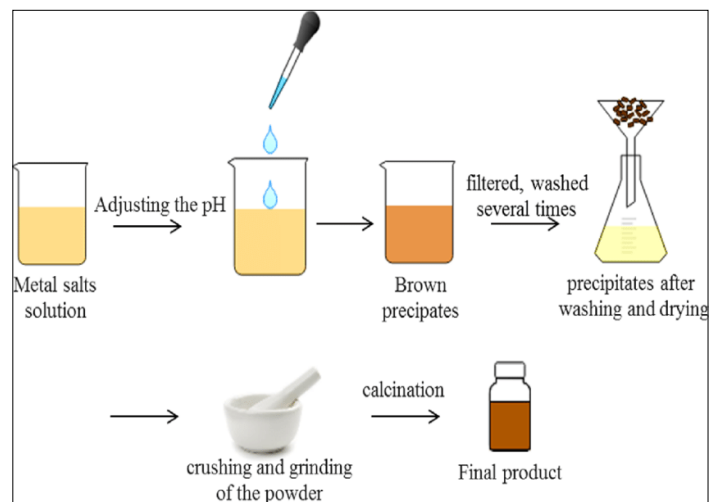


Figure 2.1 Synthesis of spinel ferrite nanoparticles by co-precipitation method. [3]

2.1.2 Spray pyrolysis method

Spray pyrolysis method is based on forming an aerosol from various precursor solutions, which could be a solution of metallic salts or a colloidal solution. The generated solution droplets (aerosol) are then rapidly heated in a furnace at given temperature, thus passing

through several stages: (1) evaporation of the solvent from the surface of the droplets, (2) drying the droplets containing the precipitated solute, (3) the annealing of the precipitate at high temperatures (thermolysis), (4) formation of microporous particles of defined phase composition, (5) formation of solid particles, and (6) sintering of solid particles. The particles obtained after thermolysis are very reactive and hence inner (“in situ”) sintering is needed. In this procedure, preparation of uniform and fine droplets of reactants and their controlled thermal decomposition are demanding operations. Figure 2.2 shows the schematic diagram of experimental setup used in this method. [5]

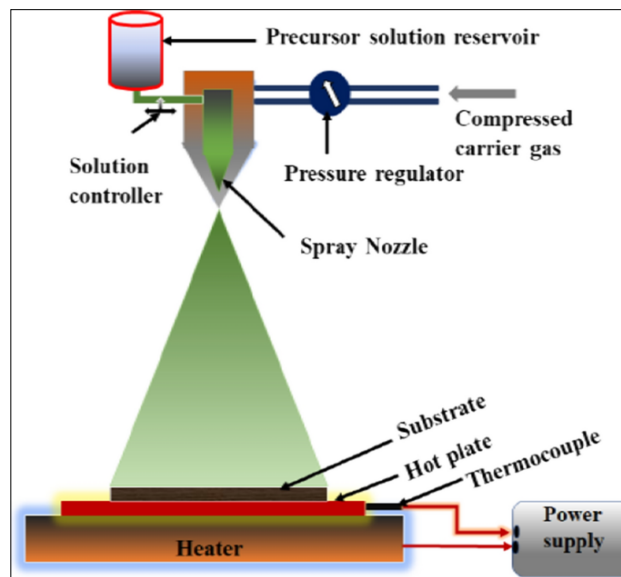


Figure 2.2 Schematic diagram of Spray Pyrolysis Method

Advantages:

1. Spray pyrolysis is very efficient, cost effective, and utilizes simple equipment.
2. The thin films produced have large surface area of substrate coverage and potential and homogeneity of mass synthesis.

Disadvantages:

1. spray pyrolysis seems not useful due to poor quality of thin film, thermal decomposition, and vapor convection.
2. It is not easy to scale-up (yield is very low).

3. Oxidation of sulphides when processed in air atmosphere is possible. ^[5,6]

2.1.3 Sol-Gel method:

Sol-Gel method provides a new approach to the preparation of new materials which allows a better control of the whole reactions involved during the synthesis of solids. It is a more chemical method (wet chemical method) for the synthesis of various nanostructures, especially metal oxide nanoparticles. The molecular precursor (usually metal alkoxide) is dissolved in water or alcohol and converted to gel by heating and stirring by hydrolysis or alcoholysis respectively. The gel obtained from the hydrolysis/alcoholysis process is wet or damp and has to be dried using appropriate methods depending on the desired properties and application of the gel. For example, if it is an alcoholic solution, the drying process is done by burning alcohol. After this stage, the produced gels are powdered and then calcined. The sol-gel method is a conventional and industrial method for the synthesis of nanoparticles with different chemical composition. The basis of the sol-gel method is the production of a homogeneous sol from the precursors and its conversion into a gel. The solvent in the gel is then removed from the gel structure and the remaining gel is dried and by grinding the gel by special mills, it is possible to achieve nanoparticles. At room temperature there is good control over the chemical composition of the products. The sol-gel method can be used in the process of making ceramics as a moulding material and can be used as an intermediate between thin films of metal oxides in various applications. The materials obtained from the sol-gel method are used in various optical, electronic, energy, surface engineering, biosensors, and pharmaceutical and separation technologies (such as chromatography). ^[7] Figure 2.3 shows the schematic diagram of experimental setup used in this method.

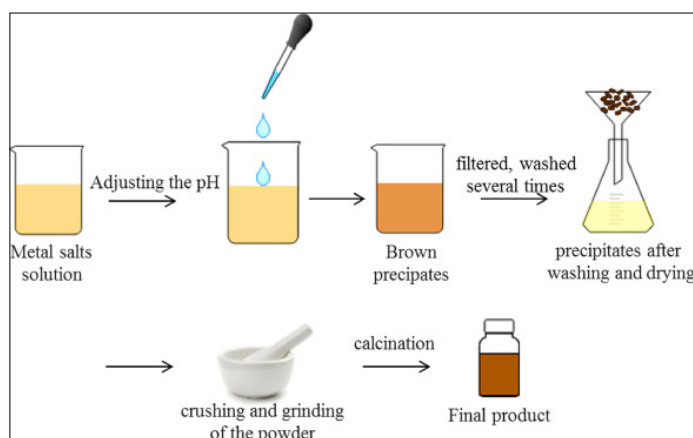


Figure 2.3 Schematic diagram of Sol-Gel Method ^[3]

Advantages:

1. The sol-gel method is a cost-effective method.
2. Due to the low reaction temperature, there is good control over the chemical composition of the products.
3. Has good possibility of obtaining better size and morphological control.

Disadvantages:

1. Presence of large concentrations of pores and the removal of undesirable residuals like hydroxyls and organics.
2. High cost of raw materials and the long processing times. ^[7,8]

2.1.4 High Energy Ball Milling method:

Ball milling is a mechanical technique that is broadly used to grind powders into fine particles. The reactants are generally broken apart using solvent molecules in the traditional method; but in ball milling, reactants are broken by using mechanical forces. Hence it is a mechanical synthesis method to produce materials that are milled to extremely fine powders. Milling temperature, type of mill, milling speed etc. are the factors that need to be considered when using ball milling as a synthesis method. It is an ecologically friendly

synthesis method as it doesn't need any solvents in the process, although solvents can be used.^[9] The fine powder produced from ball milling can be consolidated to bulk form for large-scale applications such as hip implants and bone screws. Usually, the fine powders are compacted and sintered together via methods like hot isostatic pressing and explosive compaction under the temperatures or conditions that suppress grain growth and maintain nanocrystalline microstructure. Bulk metallic materials produced by this approach have achieved the theoretical densities of nanocrystalline materials and greatly improved mechanical properties compared to their conventional, micron-grained counterparts.^[10,11]

Figure 2.4 shows the High Energy Ball Milling method.

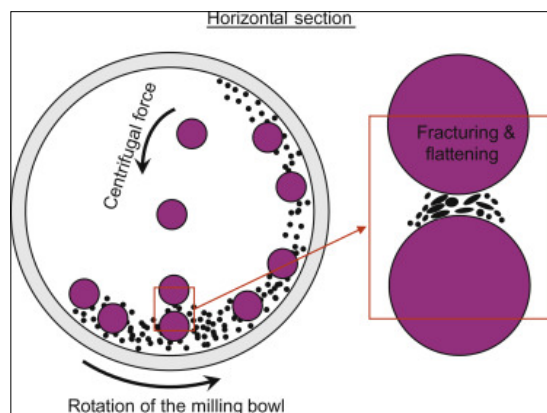


Figure 2.4 High Energy Ball Milling Method

Advantages:

1. Particles of 2 to 20 nm in size can be produced. The size of particles also depends upon the speed of the rotation of the balls.
2. It is an inexpensive and easy process.

Disadvantages:

1. As the process is not so sophisticated, therefore the shape of the nanomaterial is irregular.
2. There may be contaminants inserted and also produces crystal defects.^[10]

2.1.5 Combustion Method:

The combustion method is a material preparation method that has gained popularity in the academic and industrial fields due to its simple and economical procedure for the preparation of advanced ceramics, catalysts and nanomaterials. It offers a flexible approach of obtaining nanomaterials. It is also known as self-propagating high temperature synthesis since the desired inorganic material is formed by exothermic combustion reactions. It follows a process of bringing a saturated aqueous solution of the desired metal salts and a suitable organic fuel to boil, until the mixture ignites and a rather faster combustion reaction takes off, resulting in a dry, usually crystalline and fine particle oxide powder. To produce a mixed oxide, the mixture containing the desired metal ions, in the form of water-soluble nitrate salts and a fuel such as urea can be used. These reactions are exothermic in nature and often lead to explosive conditions if not controlled. The Combustion of metal nitrates-urea mixture usually occurs as a self-propagating and nonexplosive exothermic reaction, large amounts of gases formed can result in the appearance of a flame, which can reach a temperature in excess of 1000°C. By simple calcinations, the metal nitrates can be decomposed into metal oxides upon heating to or above the phase transformation temperature. A constant external heat supply is necessary in this case, to maintain the system at the high temperature required to accomplish the phase transformation temperature. Figure 2.5 shows the schematic diagram of the experimental setup used in this method. Following are the steps taking place in the combustion process. (1) The oxidant, fuel and dopant are mixed with help of a suitable solvent and then stirred for homogenization. (2) The mixture is kept in a furnace or hot plate initially and the ignition of a flame is observed. Once the combustion process is initiated, the process is self-propagated by the energy of an exothermic redox reaction. (3) When the whole mixture is heated uniformly, the mixture can be taken out of the furnace and crushed well to get powder form.^[12]

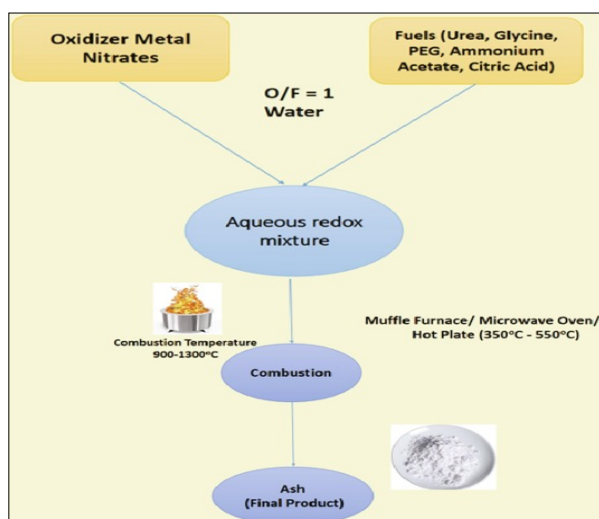


Figure 2.5 Schematic diagram of Combustion method. [12]

Advantages:

1. The purity of material is very high and highly homogenous.
2. Once the initialization of the method is needed, then the process becomes self-sustaining i.e., it becomes automatic process.
3. The morphology can be controlled.

Disadvantages:

1. If the reactants have very different precipitation rates this method may not work.
2. There is a probability of trace impurities to get precipitated with the product.
3. Time consuming.

2.1.6 Hydrothermal Method

In the process of continuous development of materials science, the research and development of new processes for material preparation and synthesis has always been a crucial part. Many researchers have been searching for a material synthesis method with limited pollution, easy operation, excellent product performance, and low production cost.

The synthesis methods of inorganic powder materials mainly include the solid phase, liquid phase, and gas phase methods. The solid phase method results in a high yield and is easy to

realize for large-scale industrial production. However, because of the limitations of the equipment and the process itself, it is difficult to control the particle size, purity, and morphology of powder using the solid phase method. The liquid phase method mainly includes the precipitation, hydrothermal, colloidal, and sol-gel methods. The advantages of the liquid phase method are convenient operation, simple synthesis process, and controllable particle size. However, most liquid phase methods consume more energy and have high costs. The gas phase process generally includes the evaporation-condensation and chemical vapor phase reaction methods. The particles prepared using the gas phase method are small in size, have a high uniform purity, and have high surface activity and good dispersibility, but equipment and a large amount of solvent is required during the reaction process, making it difficult to produce at a large scale.^[13]

The hydrothermal method is a promising liquid phase preparation technology that has developed rapidly during recent years.^[13]

Hydrothermal synthesis refers to the synthesis of substances via chemical reactions in a sealed and heated solution above ambient temperature and pressure. The concept 'hydrothermal' originates from earth science, where it implies a regime of high temperatures and water pressures. Highly crystalline spinel ferrite nanoparticles can be precisely developed by following this method. Moreover, hydrothermal synthesis methodology maintains a good control on porosity and composition. Materials exhibiting high vapor pressure near the melting point are believed to form nanoparticles only by this method. This method has gained attention in various fields and is widely used in many fields, such as the piezoelectric, ferroelectric, ceramic powder, and oxide film fields. ^[13,14]

Advantages:

1. Synthesize substances that are unstable near the melting point.

2. Has ability to produce large crystals of high quality.
3. The ability to generate crystalline phases which are not stable at the melting point.

Disadvantages:

1. Expensive and High pressure, special reactor (autoclave) required.
2. The slurry formed is highly corrosive. ^[3,14,15]

Zinc Ferrite Preparation by Hydrothermal Method:

Metal salts as Zinc Acetate, Ferric Nitrate were weighed along with CTAB. 10g of NaOH was weighed and dissolved in 125ml of distilled water. All the precursors were taken in stoichiometric ratios to meet the requirement of the particular concentration. CTAB was weighed equal to the mass of the mass of zinc acetate plus the mass of ferric nitrate. After weighing the reactants were carefully poured into a 400ml beaker containing 100ml of distilled water. The resultant solution was subjected to heat with constant stirring. A specially designed electric stirrer was used to obtain a homogeneous mixture of the solution. A magnetic stirrer was not used in this case as its angular frequency changes with an increase in temperature which will resist us from obtaining the desired outcome. After continuous stirring for about 1 hour the volume of the mixture raised to about 200ml and the solution became little thick. At this stage freshly prepared aqueous NaOH was added to the solution dropwise till the we attained the pH of 11 of the solution. The solution was then transferred to an autoclave, sealed and kept in oven for 12 hours at 180°C. After 12 hours the solution from the autoclave was removed and filtered with HCl and distilled water for around 5 times. After filtering with HCl and distilled water the solution was filtered with ethanol at once. Then the filtered sample was kept in oven at 80°C for 8 hours. The sample was then crushed and grinded to get powdered Zinc Ferrite nanoparticles. The flow chart of the followed method is shown in Figure 2.6.

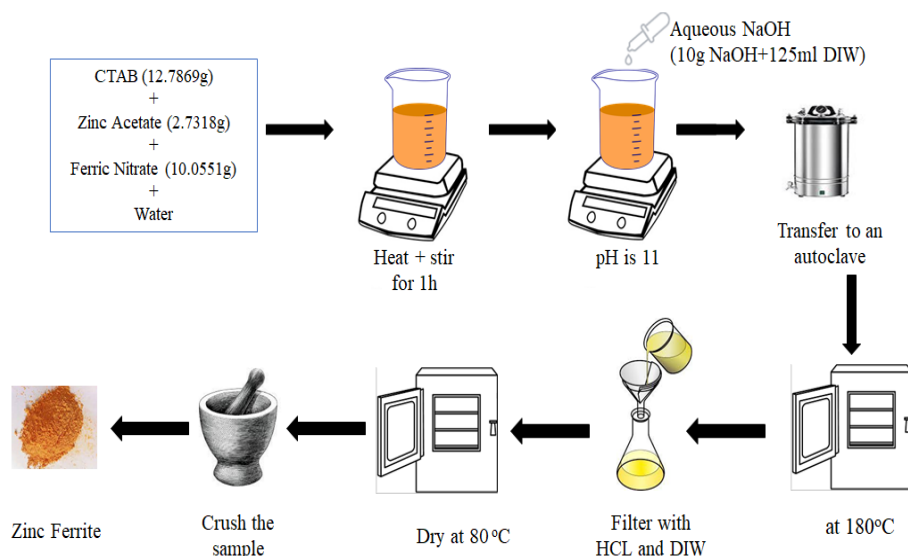


Figure 2.6 Flow chart of Hydrothermal method.

2.2 Methods of preparation of Graphene Oxide nanoparticles.

2.2.1 Hofmann's Method

The preparation of graphite oxide by the Hofmann method is known for a long time. In this method, pure graphite used as a precursor is further oxidized by potassium chlorate in strongly acidic environment. Hence follows a chlorate route.

In this method mixture of sulfuric acid and nitric acid is added to a reaction flask containing a magnetic stirrer. The mixture is then cooled using an ice bath for about 30 min. Under vigorous stirring Graphite is added to the mixture. While keeping the reaction flask in the ice bath, potassium chlorate is added slowly to the mixture. After the complete dissolution of potassium chlorate, the reaction flask is then loosely capped to allow the escape of the gas evolved and the mixture is continuously stirred for 96 hours at room temperature. The mixture is then decanted using deionized water. Graphene oxide is then redispersed in HCl solution to remove sulphate ions and repeatedly centrifuged and redispersed in deionized water until a negative reaction on chloride and sulphate ions was achieved. Graphene oxide slurry was then dried in a vacuum oven. This sample is termed as HO-GO. Similarly

modified Hofmann's method works as same as above. Here the reaction flask is kept under continuous stirring for only 2 hours to allow the escape of the gas evolved. This sample is termed as HO-GO-FAST. ^[16,17] Figure 2.7 shows the schematic diagram of this method.

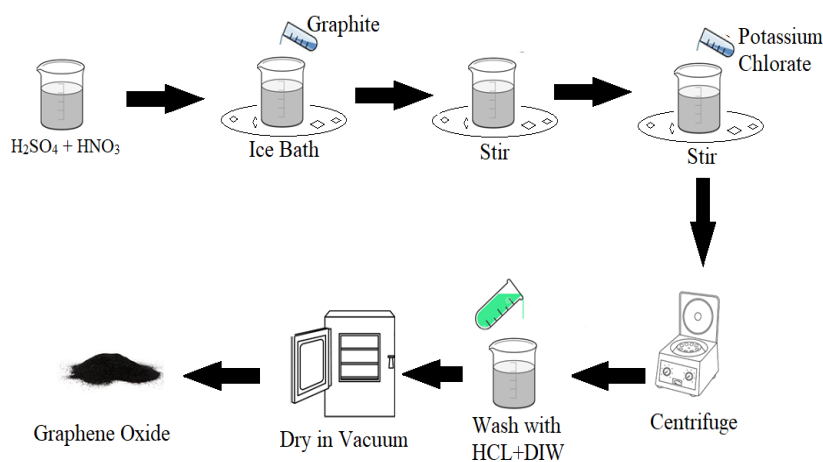


Figure 2.7 Schematic diagram of Hofmann's method.

2.2.2 Staudenmaier's Method

Staudenmaier's method goes hand in hand with the Hofmann's method. This method also follows the chlorate route. Firstly sulfuric acid and fuming nitric acid are added to a reaction flask containing a magnetic stir bar. The mixture is then cooled by immersion in an ice bath for 30 min. Graphite is then added to the mixture with vigorous stirring motion to avoid agglomeration and to obtain a homogeneous dispersion. While keeping the reaction flask in an ice bath, potassium chlorate is slowly added to the mixture (over a 30 min period) in order to avoid a sudden increment in temperature and the formation of explosive chlorine dioxide gas. Upon the complete dissolution of potassium chlorate, the reaction flask is then loosely capped to allow the escape of the gas evolved and the mixture was continuously stirred vigorously for 96 h at room temperature. On completion of the reaction, the mixture was then poured into deionized water and decanted. Graphite oxide was then redispersed in HCl solutions to remove sulphate ions and repeatedly centrifuged and redispersed in deionized water until a negative reaction on chloride and sulphate ions (with $AgNO_3$ and

Ba(NO₃)₂ respectively) was achieved. Graphite oxide slurry was then dried in a vacuum oven at 60 °C for 48 h before use. ^[17] Figure 2.8 shows the schematic diagram of this method.

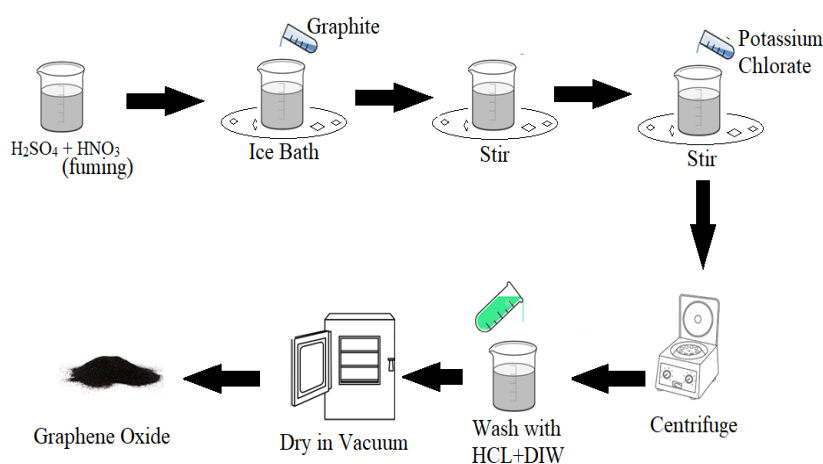


Figure 2.8 Schematic diagram of Staudenmaier's method.

2.2.3 Tour's Method

Graphene oxide colloidal solution is synthesised by the modified Tour method. In this method Graphite powder is added to sulphuric acid and cooled to 0 °C with continuous stirring for 4 h. Potassium permanganate is then added in the next step at a solution temperature of less than 5 °C with stirring for roughly around 30 min. The resulting mixture is heated further to 35 °C–40 °C for 2 h. Dropwise water is added, and the mixture is kept at room temperature for 2 h with continuous stirring. Water is added gradually again and followed by hydrogen peroxide until the colour of the solution changed to yellow, with further stirring for 30 min. At this stage, aqueous NaOH solution is added increasing the pH to 2.0–2.2, which is the main change in the GO synthesis protocol developed by the Tour group. A possible effect can be explained by the adsorption of OH⁻ anions on graphene stacking layers with an increase in the concentration of hole-like defects, which leads to a decrease in the size of negatively charged particles with a subsequent increase in their colloidal stability and oxidation efficiency. An excessive amount of sulphuric acid can negate the possibility of adsorption of Na⁺ ions on GO sheets with the reduction of the open epoxy

surface group. The resulting solution is further ultrasonicated for 1 h followed by centrifugation. The material is then washed with distilled water, HCl solution and ethanol until a pH value of about 6.5–7.0 is reached. Further the material is dried to get powdered Graphene Oxide. Figure 2.9 shows the schematic diagram of experimental setup used in this method. ^[18]

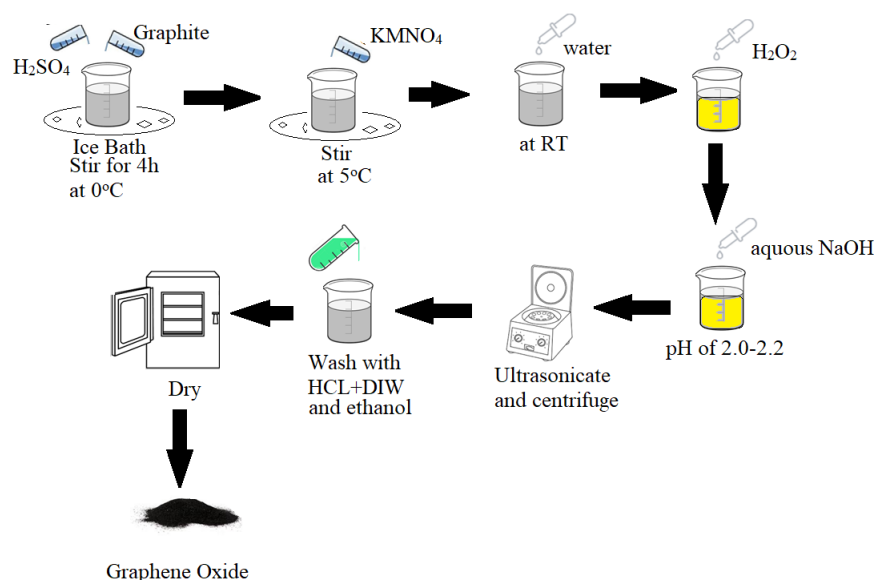


Figure 2.9 Schematic diagram of Tour's method.

2.2.4 Modified Hummer's Method

The most important and widely used method for the synthesis of graphite oxide is the one developed by Hummers 1958 (Hummers' method). ^[19,20] It consists of carrying out a reaction of graphite powder with KMnO₄ and NaNO₃ in concentrated H₂SO₄. H₂SO₄ is used to disperse graphite and a mixture of KMnO₄ and NaNO₃ as oxidant agent. The temperature is about 45 °C and the reaction time was just a few minutes long. Basically, the reaction take place in an acid solution and the addition of hydrogen peroxide (H₂O₂) make it easier to remove the metal salts. This method produces explosive exothermic reactions and generate toxic gases such as NO₂, N₂O₄, and ClO₂ during the reaction, besides, residual Na⁺ and NO₃ ions are difficult to be removed during the procedures of rinsing and purifying the graphene oxide. ^[19]

In 2010 Marcano *et al* ^[19,20] improved the Hummers' method by excluding NaNO_3 , increasing the KMnO_4 oxidants, and performing the reaction in a mixture of $\text{H}_2\text{SO}_4/\text{H}_3\text{PO}_4$ in volume proportion 9:1. This modification was successful in increasing the reaction yield and reducing the toxic gases production. Thus, a complete oxidation of graphite can be achieved using a mixture of $\text{KMnO}_4/\text{H}_2\text{SO}_4$ forming a graphite bisulphate product in which every single-layer of graphene is sandwiched by the layers of bisulphate ions. ^[19,20,21] The complete intercalation of bisulphate ions ensures the effective infiltration of the KMnO_4 solution among the graphene layers for their surface oxidation.

Since here NaNO_3 is not used as oxidant agent, the reaction produces no toxic gases such as the ones mention above. The reaction between H_2SO_4 and KMnO_4 as oxidant agent is a dissociation reaction. Continuing with the rinsing procedure, the mixture is let to cool down to room temperature. Further H_2O_2 is added to the mixture to make easier the removal of metal salts such as permanganate and manganese residuals from the mixture, now this solution turns to a bright yellow colour. The solution is then centrifuged and the supernatant is decanted away. Later the mixture is dried in oven overnight to get Graphene oxide. ^[20]

Advantages:

1. Possess very different properties and electrochemical characteristics from those produced using the Staudenmaier and Hofmann methods.
2. Low cost and toxic gas free method.

Disadvantages:

1. Time consuming
2. Require careful handling of acids

Graphene Oxide Preparation by Modified Hummer's Method:

Here pure graphite flakes were used to get Graphene Oxide (GO). 27ml of sulphuric acid (H_2SO_4) and 3ml of Phosphoric acid (H_3PO_4) (volume ratio 9:1) were mixed together in a beaker and stirred for several minutes. Then 0.225g of graphite flakes was weighed and carefully poured into the acid mixture under stirring condition and kept for stirring for several minutes. Then 1.32g of potassium permanganate (KMnO_4) was weighed and poured carefully and slowly into the solution. This mixture was stirred for 6 hours until the solution became dark green. Further 0.675ml of hydrogen peroxide (H_2O_2) was added slowly to the mixture to eliminate excess of KMnO_4 and stirred for around 10 minutes. The exothermic reaction occurred and hence ice bath was used to let the solution to cool down. 10ml of HCl and 30ml of distilled water was added and centrifuged at 2000 rpm for around 10 minutes. Then the supernatant was decanted away and residuals were then rewashed again with HCl and distilled water for more 3 times. The prepared GO solution was dried using oven at 90°C for 24 hours to produce the GO powder. Figure 2.10 shows the flow chart of the method used.

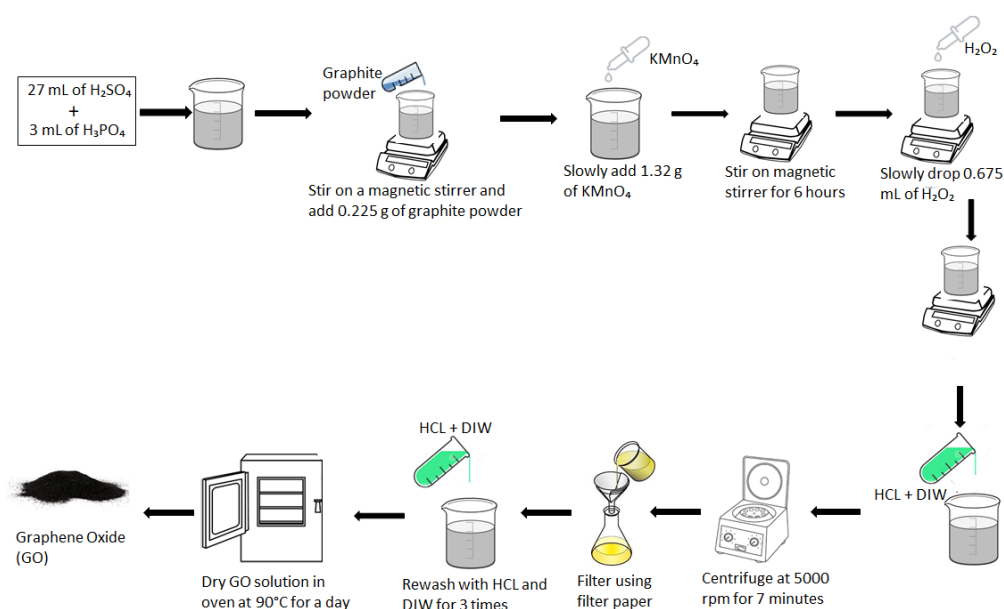


Figure 2.10 Flow chart of modified Hummer's method.

2.3 Method of preparation of Zinc Ferrite-Graphene Oxide nanocomposite.

Zinc Ferrite-Graphene Oxide Nanocomposite Preparation by Hydrothermal Method:

Three samples of ZnFe₂O₄-GO nanocomposites were prepared by varying composition of as prepared Graphene Oxide nanoparticles as 50mg, 75mg, and 100mg in as prepared Zinc Ferrite nanoparticles.

A measured quantity of 50mg of graphene oxide was dispersed in 100ml of distilled water using an ultrasonicator. Metal salts as Zinc Acetate, Ferric Nitrate were weighed along with CTAB. 10g of NaOH was weighed and dissolved in 125ml of distilled water. All the precursors were taken in stoichiometric ratios to meet the requirement of the particular concentration. CTAB was weighed equal to the mass of the mass of zinc acetate plus the mass of ferric nitrate. After weighing the reactants were carefully poured into a 400ml beaker containing 100ml of distilled water. The resultant solution was subjected to heat with constant stirring. A specially designed electric stirrer was used to obtain a homogeneous mixture of the solution. A magnetic stirrer was not used in this case as its angular frequency changes with an increase in temperature which will resist us from obtaining the desired outcome. After continuous stirring for about 1 hour the volume of the mixture became little thick. At this stage freshly prepared aqueous NaOH was added to the solution dropwise till the we attained the pH of 11 of the solution. The solution was then transferred to an autoclave, sealed and kept in oven for 12 hours at 180°C. After 12 hours the solution from the autoclave was removed and filtered with HCl and distilled water for around 5 times. After filtering with HCl and distilled water the solution was filtered with ethanol at once. The filtered sample was kept in oven at 80°C for 8 hours. The sample was then crushed and grinded to get powdered ZnFe₂O₄/GO_{50mg} nanocomposite. The same procedure as above was followed to prepare ZnFe₂O₄/GO_{75mg} and ZnFe₂O₄/GO_{100mg} nanocomposites using 75mg GO in

100ml distilled water and 100mg GO in 100ml distilled water respectively. The flow chart of the followed method is shown in Figure 2.11.

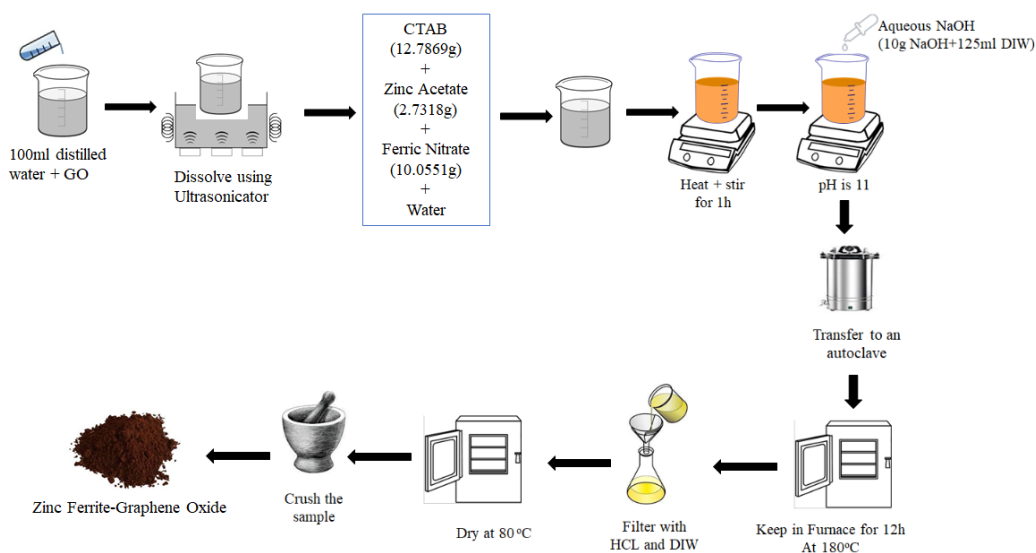


Fig 2.11 Flow chart of Hydrothermal method to prepare $ZnFe_2O_4/GO$ nanocomposites.

2.4 Glimpses of the sample preparation process

Preparation of Graphene Oxide:

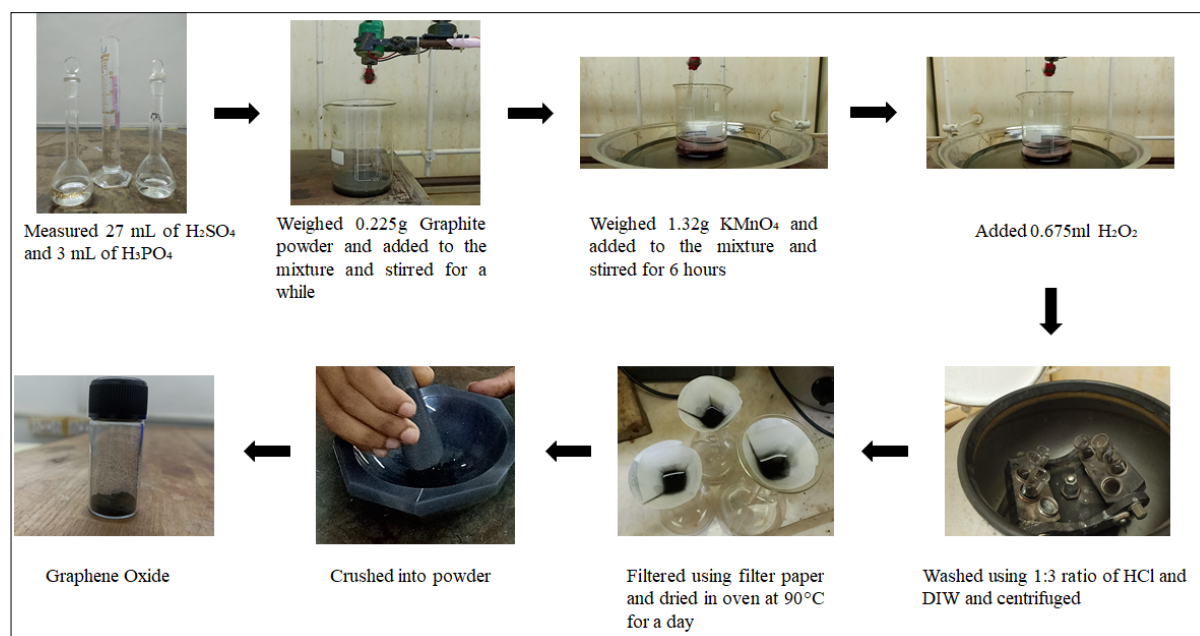


Figure 2.12 Glimpses of Graphene Oxide preparation process

Preparation of Graphene Oxide Zinc Ferrite nanocomposite:

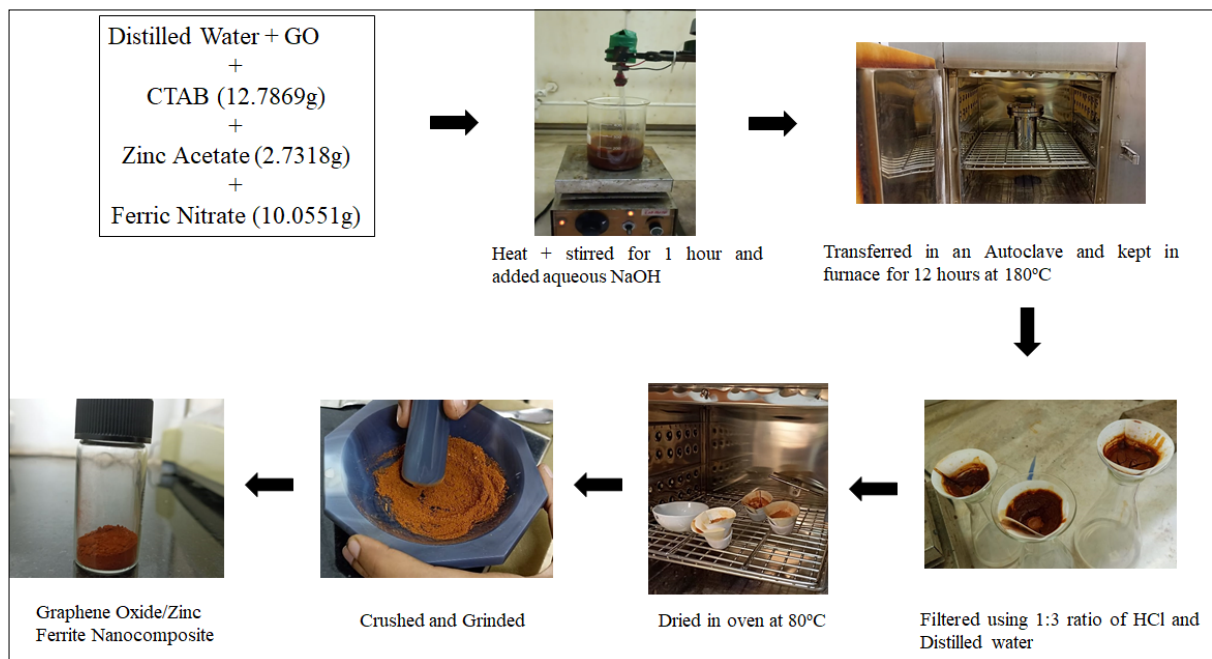


Figure 2.13 Glimpses of Graphene Oxide/Zinc Ferrite preparation process

2.5 References

1. Cele, T. (2019). Preparation of Nanoparticles. *Engineered Nanomaterials*.
2. Cruz, I. F., Freire, C., Araujo, J. P., Pereira, C., & Pereira, A. M. (2018). Chapter 3 - Multifunctional Ferrite Nanoparticles: From Current Trends Toward the Future. *Magnetic Nanostructured Materials*.
3. Soufi, A., Hajjaoji, H., Elmoubarka, R., Abdennouri, M., & Qourzal, S. (2021). Spinel ferrites nanoparticles: Synthesis methods and application in heterogeneous Fenton oxidation of organic pollutants – A review. *Applied Surface Science Advances*.
4. Rane, A. V., Kanny, K., Abitha, V. K., & Thomas, S. (2021). Chapter 5 - Methods for Synthesis of Nanoparticles and Fabrication of Nanocomposites. *Synthesis of Inorganic Nanoparticles*.
5. Gavrilovic, T. V., Jovanovic, D. J., & Dramicanin, M. D. (2018). Chapter 2 - Synthesis of Multifunctional Inorganic Materials: From Micrometer to Nanometer Dimensions. *Nanomaterials for Green Energy*.
6. Tahir, M. B., Rafique, M., Rafique, M. S., Nawaz, T., Rizwan, M., & Tanveer, M. (2020). Chapter 8 - Photocatalytic nanomaterials for degradation of organic pollutants and heavy metals. *Nanotechnology and Photocatalysis for Environmental Applications*.
7. Bokov, D., Jalil, A. T., Chupradit, S., Suksatan, W., Ansari, M. J., Shewael, I. H., . . . Kianfar, E. (2021). Nanomaterial by Sol-Gel Method: Synthesis and Application. *Advances in Materials Science and Engineering*.
8. Mackenzie, J. D. (1988). Applications of the sol-gel process. *Journal of Non-Crystalline Solids*.

9. Karttunen, A. (2022). Ball milling as a synthesis method. *Solid-state Synthesis Methods*.
10. Amsh. (n.d.). Ball Milling method for synthesis of nanomaterials. *NanoTechnology*.
11. Yang, L. (2015). 2 - Nanotechnology-enhanced metals and alloys for orthopedic implants. *Nanotechnology-Enhanced Orthopedic Materials*.
12. Parauha, Y. R., Sahu, V., & Dhoble, S. (2021). Prospective of combustion method for preparation of nanomaterials: A challenge. *Materials Science and Engineering: B*.
13. Yang, G., & Park, S.-J. (2019). Conventional and Microwave Hydrothermal Synthesis and Application of Functional Materials: A Review.
14. Dahiya, M. S., Tomer, V. K., & Duhan, S. (2018). 31 - Metal–ferrite nanocomposites for targeted drug delivery. *Applications of Nanocomposite Materials in Drug Delivery*.
15. MODAN, E. M., & PLĂIAȘU, A. G. (2020). Advantages and Disadvantages of Chemical Methods in the Elaboration of Nanomaterials.
16. Dr. Ondřej Jankovský, A. J., Luxa, J., Sedmidubský, P. D., Pumera, P. M., & Sofer, P. Z. (2017). Fast Synthesis of Highly Oxidized Graphene Oxide.
17. Poh, H. L., Šaněk, F., Ambrosi, A., Zhao, G., Sofer, Z., & Pumera, M. (2012). Graphenes prepared by Staudenmaier, Hofmann and Hummers methods with consequent thermal exfoliation exhibit very different electrochemical properties. *Nanoscale*.
18. Kotsyubynsky, V. O., Boychuk, V. M., Budzulyak, I. M., Rachiy, B. I., Hodlevska, M. A., Kachmar, A. I., & Hodlevsky, M. A. (2021). Graphene oxide synthesis using

modified Tour method. *Advances in Natural Sciences: Nanoscience and Nanotechnology*.

19. Marcano, D. C., Kosynkin, D. V., Berlin, J. M., Sinitskii, A., Sun, Z., Slesarev, A., . . . Tour, J. M. (2010). Improved Synthesis of Graphene Oxide. *ACS Nano*.
20. Santamaría-Juárez, G., Gómez-Barojas, E., Quiroga-González, E., Sánchez-Mora, E., Quintana-Ruiz, M., & Santamaría-Juárez, J. D. (2020). Safer modified Hummers' method for the synthesis of graphene oxide with high quality and high yield. *Materials Research Express*.
21. Avdeev, V., Monyakina, L., Nikol'skaya, I., Sorokina, N., & Semenenko, K. (1992). The choice of oxidizers for graphite hydrogenosulfate chemical synthesis. *Carbon*.

CHAPTER 3: CHARACTERISATION TECHNIQUES

3.1 X-ray Powder Diffraction

3.1.1 Introduction

X-rays are a form of electromagnetic radiations having high energy and shorter wavelength which can pass through most of the objects. In 1912, Max von Laue discovered that crystalline substances act as three-dimensional diffraction gratings for X-ray wavelengths similar to the spacing of planes in a crystal lattice. X-ray diffraction has now become common technique for the study of crystal structures and atomic spacing. It can be used to determine either the lattice parameters, arrangement of individual atoms in a single crystal, or the phase analysis in case of polycrystalline materials. With the knowledge of XRD and crystallography, it is possible to determine the crystal structure and molecular formula of a crystalline compound.



Figure 3.1 X-Ray Diffractometer

3.1.2 Basic Principle

X-ray diffraction is based on constructive interference of monochromatic X-rays and a crystalline sample. These X-rays are generated by a cathode ray tube which are filtered to produce monochromatic radiation, collimated to concentrate, and directed toward the sample. The interaction of the incident rays with the sample produces constructive interference when conditions satisfy Bragg's Law.

Bragg's Law:

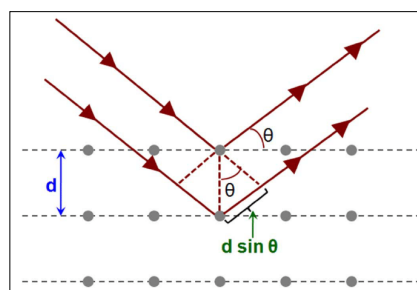


Fig 3.2 Bragg's Law ^[3]

Where n is an integer, λ is the wavelength, d is the interplanar spacing and θ is the diffraction angle. The intensity of the diffracted x-rays is measured and plotted as a function of diffraction angle 2θ . From the 2θ values of the peaks, the lattice spacing (d) values are calculated using Bragg's law. Bragg's law relates the wavelength of electromagnetic radiation to the diffraction angle and the lattice spacing in a crystalline sample. These diffracted X-rays are then detected, processed and counted. By scanning the sample through a range of 2θ angles, all possible diffraction directions of the lattice could be attained due to the random orientation of the powdered material. Conversion of the diffraction peaks to d -spacings allows identification of the material because each material has a set of unique d -spacings. Typically, this is achieved by comparison of d -spacings with standard reference patterns. A key component of all diffraction is the angle between the incident and diffracted rays. ^[1,2]

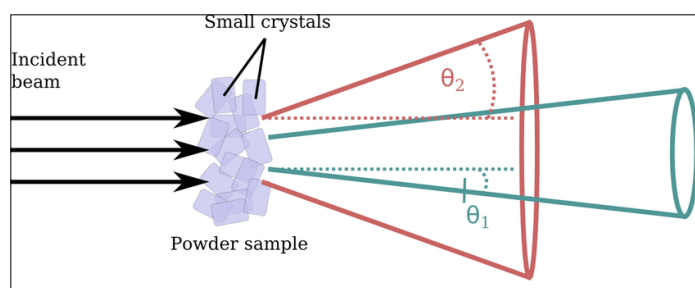


Figure 3.3 A beam of X-rays directed at a crystal forming a cone ^[4]

3.1.3 Instrumentation

X-ray diffractometers basically consist of three basic elements such as an X-ray tube, a sample holder, and an X-ray detector. X-rays are generated in a cathode ray tube by heating a filament to produce electrons which are accelerated towards a target by applying a voltage, and bombarding the target material with electrons. When electrons have sufficient energy to dislodge inner shell electrons of the target material, characteristic X-ray spectra are produced. These spectra consist of several components, the most common being K_{α} , K_{β} and K_{γ} . K_{α} radiation has high intensity and is commonly used for diffraction studies. The wavelength of this radiation for a typical copper metal target is 1.54056 Å. These X-rays are collimated and directed onto the sample. As the sample and detector are rotated, the intensity of the reflected X-rays is recorded. When the geometry of the incident X-rays impinging the sample satisfies the Bragg Equation, constructive interference occurs and a peak in intensity occurs. A detector records and processes this X-ray signal and converts the signal to a count rate which is then output to a device such as a printer or computer monitor. ^[1,2]

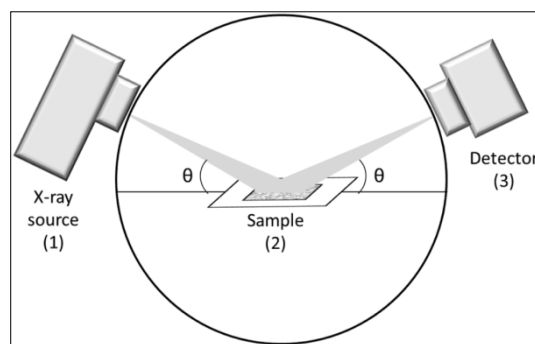


Figure 3.4 Instruments for powder X-ray diffraction have three major components: 1) X-ray source; 2) sample holder; and 3) detector. ^[5]

The simplest and most widely used method for estimating crystallite size is from the Full Width at Half Maximum (FWHM) of a diffraction peak by Debye-Scherrer's formula which

is given by . Where 'D' is the crystallite size, λ is the wavelength of the X-ray radiation, β is the angular width which is equal to the (FWHM). Also, the lattice parameter (a) is then computed by assuming cubic symmetry that is when

3.2 Scanning Electron Microscopy

3.2.1 Introduction

In 1937 Mafred von Ardenne made the Scanning Electron Microscope (SEM) with an aim to surpass and reduce the problems of chromatic aberrations images produced by the Transmission Electron Microscope. [6] The primary function of the SEM is to enlarge small features or objects otherwise invisible to human sight. It does that by way of using electron beam rather than light which is used to form images in optical light microscopes. The images are obtained by scanning an electron beam of high energy on the sample surface, hence the name scanning electron microscope. By virtue of its smaller wavelength, electrons are able to resolve finer features/details of materials to a much greater extent compared with optical light.



Figure 3.5 Carl Zeiss Scanning Electron Microscope Setup

3.2.2 Basic Principle

The SEM uses emitted electrons unlike the Transmission Electron Microscope which uses transmitted electrons. It works on the principle of applying kinetic energy to produce signals on the interaction of the electrons. These electrons are secondary electrons, backscattered electrons, and diffracted backscattered electrons which are used to view crystallized elements and photons. Secondary and backscattered electrons are used to produce an image. The secondary electrons are emitted from the specimen play the primary role of detecting the morphology and topography of the specimen while the backscattered electrons show contrast in the composition of the elements of the specimen. [6,7]

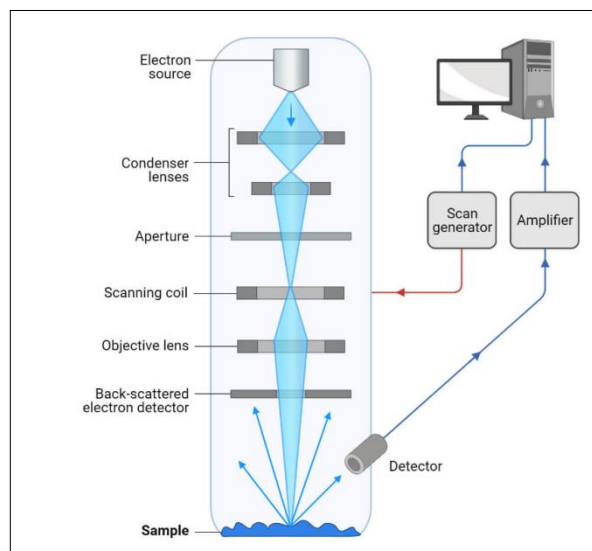


Figure 3.6 Schematic Diagram of SEM [7]

3.2.3 Instrumentation

The major components of the Scanning Electron Microscope include electron source, lenses, scanning coil, detector, display device, power supply and vacuum system.

- 1) Electron Source - This is where electrons are produced under thermal heat at a voltage of 1-40kV. These electrons condense into a beam that is used for the creation of an

image and analysis. There are three types of electron sources that can be used such as Tungsten filament, Lanthanum hexaboride, and Field emission gun (FEG)

- 2) Lenses - SEM has several condenser lenses that focus the beam of electrons from the source through the column forming a narrow beam of electrons that form a spot called a spot size.
- 3) Scanning Coil - These are used to deflect the beam over the specimen surface.
- 4) Detector - SEM is made up of several detectors that are able to differentiate the secondary electrons, backscattered electrons, and diffracted backscattered electrons. The functioning of the detectors highly depends on the voltage speed, the density of the specimen.
- 5) The display device and vacuum system - Display devices are used to get the output SEM images and vacuums are needed to prevent electrical discharge in the gun assembly (arcing), and to allow the electrons to travel within the instrument unimpeded. ^[6,7]

3.3 UV-Visible Spectroscopy

3.3.1 Introduction

Ultraviolet–visible (UV–visible) spectroscopy is primarily a quantitative analytical technique concerned with the absorption of near-UV (180–390 nm) or visible (390–780 nm) radiation by chemical species in solution. Basically it is an analytical technique that measures the amount of discrete wavelengths of UV or visible light that are absorbed by or transmitted through a sample in comparison to a reference or blank sample and is a widely used technique in many areas of science ranging from bacterial culturing, drug identification and nucleic acid purity checks and quantitation, to quality control in the beverage industry and chemical research. ^[8]

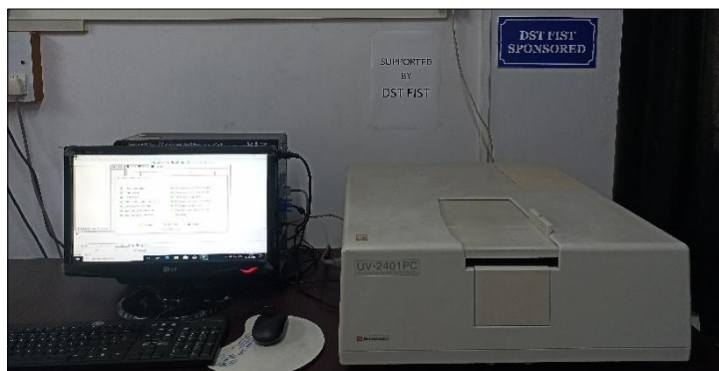


Figure 3.7 UV-Visible Spectrometer

3.3.2 *Basic principle*

Since this spectroscopy technique relies on the use of light, let's first consider the properties of light. We know that light has a certain amount of energy which is inversely proportional to its wavelength. Thus, we know that shorter wavelengths of light carry more energy and longer wavelengths carry less energy. A specific amount of energy is needed to excite electrons in a substance to a higher energy state which we can detect as absorption. Different specific amount of energy is required to promote the electrons to a higher energy state from electrons in different bonding environments. This is why the absorption of light occurs for different wavelengths in different substances. We are able to see a spectrum of visible light, from approximately 380 nm, which is violet, to 780 nm, which is red. UV light has wavelengths shorter than that of visible light to approximately 100 nm. Therefore, light can be described by its wavelength, which can be useful in UV-Vis spectroscopy to analyse or identify different substances by locating the specific wavelengths corresponding to maximum absorbance. The absorption by a molecule of UV or visible light radiation results in transition between molecule's energy level. ^[8,9]

In this thesis we have used UV-Vis Spectroscopy to determine the energy band gap E_g by plotting graph of reflectance v/s wavelength using Kubelka Munk's function i.e.,

Where,

- reflectance coefficient

- planks constant

- Frequency of the photon

- proportionality constant

- band gap energy

- denotes the nature of the electronic transition either direct or indirect allowed transition ^[8,9,10]

3.3.3 Instrumentation

There are four main components in a UV-Vis Spectrometer namely, light source, wavelength selection, sample analysis and detection. Going further to the details of each components lets refer to the figure below.

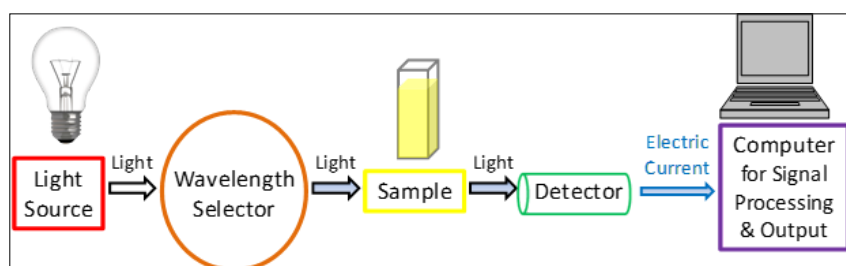


Figure 3.8 Schematic diagram of UV-Vis Spectrometer ^[9]

Light Source:

A steady source able to emit light across a wide range of wavelengths is essential as this is a light-based technique. A single xenon lamp is commonly used as a high intensity light source for both UV and visible light ranges. However, xenon lamps are associated with higher costs and are less stable in comparison to tungsten and halogen lamps. For the instruments

employing two lamps, a tungsten or halogen lamp is commonly used for visible light, while a deuterium lamp is the commonly used for UV light. As two different light sources are needed to scan both the UV and visible wavelengths, the light source in the instrument must switch during measurement. Hence in practice, this switchover typically occurs during the scan between 300 and 350 nm where the light emission is similar from both light sources and the transition can be made more smoothly.

Wavelength Selection:

Certain wavelengths of light suited to the sample type and analyte for detection must be selected for sample examination from the broad wavelengths emitted by the light source. Some available methods for this selection include: monochromators, absorption filters, interference filters, cut-off filters, bypass filters etc. Monochromators are most commonly used for this process due to their versatility. However, filters are often used together with monochromators to narrow the wavelengths of light selected further for more precise measurements and to improve the signal-to-noise ratio.

A monochromator separates light into a narrow band of wavelengths. It is most often based on diffraction gratings that can be rotated to choose incoming and reflected angles to select the desired wavelength of light.

Sample analysis:

After the wavelength selection is done in the spectrophotometer, the light then passes through a sample. Measuring a reference sample, often referred to as the "blank sample", such as a cuvette filled with a similar solvent used to prepare the sample for all analysis. If an aqueous buffered solution containing the sample is used for measurements, then the aqueous buffered solution without the substance of interest is used as the reference. For example when examining bacterial cultures, the sterile culture media would be used as the reference. The

reference sample signal is then later used automatically by the instrument to help obtain the true absorbance values of the analytes. Quartz sample holders are required for UV examination because quartz is transparent to the majority of UV light. Air may also be thought of as a filter because wavelengths of light shorter than about 200 nm are absorbed by molecular oxygen in the air. A special and more expensive setup is required for measurements with wavelengths shorter than 200 nm, usually involving an optical system filled with pure argon gas.

Detection:

A detector is used to convert the light into a readable electronic signal after the light has passed through the sample. Generally, detectors are based on photoelectric coatings or semiconductors.

A photoelectric coating ejects negatively charged electrons when exposed to light. When electrons are ejected, an electric current proportional to the light intensity is generated. A photomultiplier tube (PMT) is one of the most common detectors used in UV-Vis spectroscopy. A PMT is based on the photoelectric effect to initially eject electrons upon exposure to light, followed by sequential multiplication of the ejected electrons to generate a larger electric current. PMT detectors are especially useful for detecting very low levels of light.

When semiconductors are exposed to light, an electric current proportional to the light intensity can pass through. More specifically, photodiodes and chargecoupled devices (CCDs) are two of the most common detectors based on semiconductor technology. After the electric current is generated from whichever detector was used, the signal is then recognized as output to a computer or screen. ^[8,9]

3.4 THE SUPERCONDUCTING QUANTUM INTERFERENCE DEVICE (SQUID)

3.4.1 Introduction

The superconducting quantum interference device (SQUID) can be used as an extremely sensitive detector of magnetic flux. It consists of two parallel Josephson junctions as shown in the figure 3.9. Measurement of magnetic flux is based on two fundamental phenomena in superconductors, the Josephson effect and the fluxoid quantization, where the flux penetrating

a superconducting loop is quantized in steps of $\phi_0 = h/2e = 2.068 \cdot 10^{-15} \text{ Wb}$.^[9] SQUIDS can be used as sensitive measurement devices also for several other electrical measurements.^[9,10]

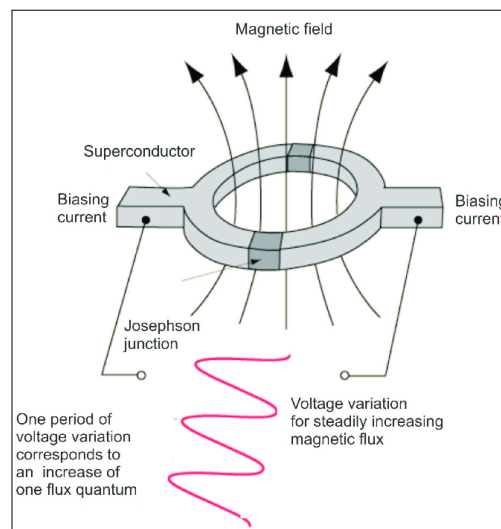


Figure 3.9 Two parallel Josephson junctions in SQUID^[9]

3.4.2 Basic Principle and Instrumentation

SQUID consists of a sensing element which is a loop of superconducting metal sunk into a bath of liquid helium as shown in figure 3.10. The loop has one or more weak links in it. Change in magnetic field will cause a current in the loop. The current increases until it reaches saturation current at the weak link and the resistance in the weak link interrupts the current in the loop. The changes in the loop are detected with nearby coil, providing a signal which is used to measure the changing magnetic field.

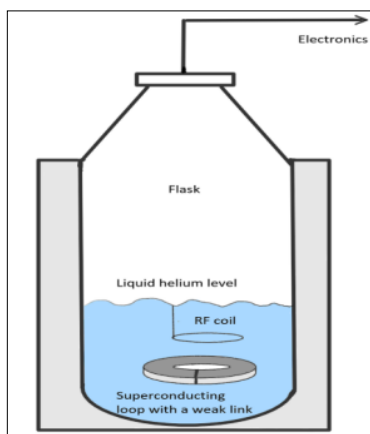


Figure 3.10 Principle of a SQUID ^[10]

SQUID instruments consist of a SQUID amplifier or a sensor and a detection circuit which converts the detected signal into a magnetic flux. These are operated as radiofrequency (RF) or direct current (DC) SQUIDs. The smallest magnetic fields that can be measured by SQUIDs are in the range from 10^{-14} to 10^{-12} T. Because of the required superconductivity and the extreme sensitivity, SQUIDs are controlled in really stable conditions in cryostat with liquid helium (4.2 K) or liquid nitrogen (77 K) for high- T_c SQUIDs. SQUID's sensitivity is high enough to image 160 nA currents at a 650 μ m working distance. ^[9,10] In our thesis here we have used SQUID for magnetic analysis of our as prepared sample by plotting magnetic moment v/s magnetic field.



Figure 3.11 SQUID

3.5 Raman Spectroscopy

3.5.1 Introduction

Raman spectroscopy belongs into the category of vibrational spectroscopy which is a powerful tool to characterize the structure of various kinds of materials. It chemically analyses the sample by using light to excite molecular vibration, and interpreting this interaction afterwards. It is based on the inelastic scattering of light that occurs when matter is irradiated by light. As the change of wavelength is very small compared to the wavelength of the irradiating light, the change of wavelength is most easily observed when using monochromatic light sources. After this monochromatic light gets interacted with the sample, a very small part of it has changed its wavelength. This is called as the Raman effect which was discovered by C.V. Raman in 1930 which opened the door to a new kind of spectroscopy which is Raman spectroscopy. Raman spectroscopy did not really take off however, until the discovery of the laser thus, the use of monochromatic light plays an important role. The sample is irradiated with a laser and some of the scattered light is analysed with a spectrograph. At the end Raman spectrum is obtained which shows the characteristic signals or “bands” for the material under investigation. ^[13]



Figure 3.12 Raman Spectrometer

3.5.2 Basic Working

In Raman spectroscopy technique, the sample is irradiated with a monochromatic laser beam which interacts with the molecules of sample and originates a scattered light. This scattered light has a frequency different from that of incident light is used to construct a Raman spectrum. Raman spectra arises due to an inelastic collision between incident monochromatic radiation and molecules of sample. When a monochromatic radiation strikes at sample, it scatters in all directions after its interaction with sample molecules. Much of this scattered radiation has a frequency which is equal to frequency of incident radiation and constitutes Rayleigh scattering. Only a small fraction of scattered radiation has a frequency different from frequency of incident radiation and constitutes Raman scattering. When the frequency of incident radiation is higher than frequency of scattered radiation, Stokes lines appear in Raman spectrum. But when the frequency of incident radiation is lower than frequency of scattered radiation, anti-Stokes lines appear in Raman spectrum. Scattered radiation is usually measured at right angle to incident radiation. ^[14,15]

Stokes shifted Raman bands involve the transitions from lower to higher energy vibrational levels and therefore, Stokes bands are more intense than anti-Stokes bands and hence are measured in conventional Raman spectroscopy while anti-Stokes bands are measured with fluorescing samples because fluorescence causes interference with Stokes bands. The magnitude of Raman shifts does not depend on wavelength of incident radiation. Raman scattering depends on wavelength of incident radiation. A change in polarizability during molecular vibration is an essential requirement to obtain Raman spectrum of sample. Since Raman scattering due to water is low, water is an ideal solvent for dissolving samples. Glass can be used for optical components in Raman spectrophotometer. ^[13,14,15]

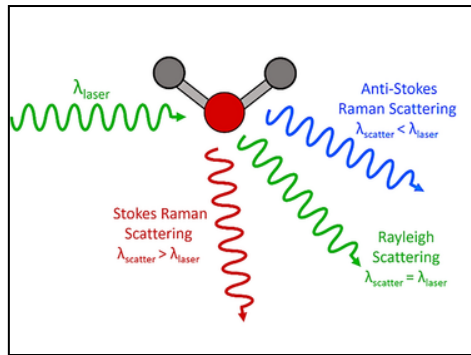


Figure 3.13 Raman scattering [17]

3.5.3 Instrumentation

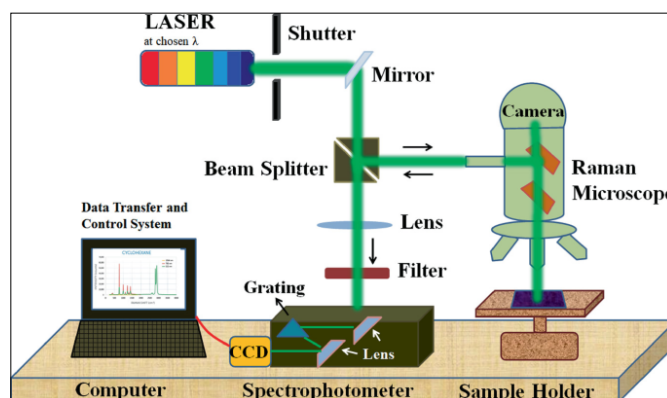
A Raman spectrometer consists of several basic components including a laser which serves as the excitation source to induce the Raman scattering. Generally, solid state lasers are used in modern Raman instruments with popular wavelengths of 532 nm, 785 nm, 830 nm and 1064 nm. The shorter wavelength lasers have higher Raman scattering cross-sections so the resulting signal is greater. For this reason, many Raman systems feature the 785 nm laser. Fibre optic cables are used to transmit and collect the laser energy from the sample by. A notch or edge filter is used to eliminate Rayleigh and anti-Stokes scattering and the remaining Stokes scattered light is passed on to a dispersion element, typically a holographic grating. A CCD detector captures the light, resulting in the Raman spectrum. Since Raman scattering yields a weak signal, it is most important that high-quality, optically well-matched components are used in the Raman spectrometer. [13,14,16]

Figure 3.14

Raman

3.6 Electrical

3.6.1 Introduction



Working of

Spectroscopy [18]

Measurements

Dielectric properties - Different dielectric materials have different and unique set of electrical characteristics which depend on their dielectric properties. These properties when measured accurately can provide valuable information incorporate the material into its intended applications for more solid designs or to monitor the manufacturing process for improved quality material. A dielectric supports charge by acquiring polarization in an electric field, whereby one surface develops a net positive charge while opposite surface develops a net negative charge. This is made possible by the presence of electric dipoles. All non-conducting materials are capable of electronic polarization hence, all insulators are dielectric to some degree. In contrast the ionic orientation modes are only available to materials possessing ions and permanent dipoles respectively. ^[19,20]

Dielectric constant - The dielectric constant of a substance or material is a measure of its ability to store electrical energy. It is an expression of the extent to which a material holds or concentrates electric flux.

Dielectric loss – an efficient dielectric supports a varying charge with minimal dissipation of energy in the form of heat. Conduction loss and dielectric loss are the two main forms of loss that may dissipate energy within a dielectric. In conduction loss a flow of charge through the material causes energy dissipation whereas dielectric loss is the dissipation of energy through the movement of charges in an alternating electromagnetic field as polarization switches direction. ^[19,20]

3.6.2 Basic working and Instrumentation.

Preparation of the sample for measurement:

The as prepared nanocomposite sample was pressed into pellets of 13mm diameter and about 2mm in thickness by applying pressure of about 3 ton. Once the pellets were formed, both faces of the pellets were painted with silver for making ohmic contacts.

Experimental technique and setup: The instrument used is basically an electrical network analyser that is used to measure an electrical network's network parameters. Currently, these instruments are normally used to measure S-parameters i.e., scattering parameters which describe the main relationships between input and output ports within an electrical system because transmission and reflection of electrical networks are very simple to calculate at high frequencies, although there are other types of network parameter sets like Y, Z & H-parameters. These analysers are frequently used to differentiate two-port networks like filters & amplifiers and filters. The basic working principle of a network analyser is to measure the phase & amplitude of both the waves like reflected and incident at the different ports of the Device Under Test (DUT). This analyser includes both a source & set of receivers. A source is used to produce a known stimulus signal whereas receivers are used to decide changes in stimulus signal which is caused by the DUT. Generally, a network analyser has the capacity to understand different protocols, which provides information regarding what is happening on a network by letting you observe the actual data that supplies packet by packet over it. It is used in transmission & reflection measurements. Transmission measurements comprise gain, insertion loss, transmission coefficient whereas reflection measurements comprise return loss, reflection coefficient, impedance, etc. The operating frequencies of these analysers range from 1 Hz -1.5 THz. These analysers can also be used for the analysis of stability for the measurement of ultrasonic, audio components, and open loops.

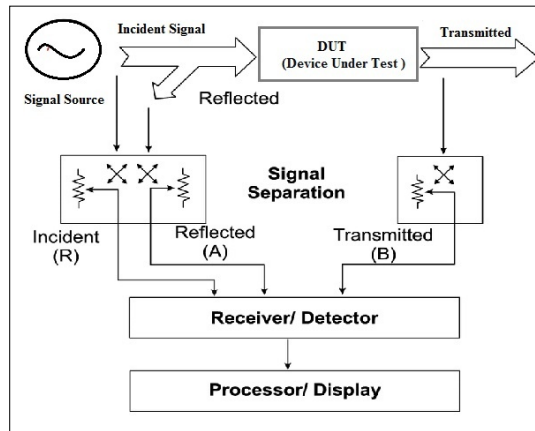


Figure 3.15 Block Diagram of Electrical Network Analyser

Network analysers are classified into three types including Scalar Network Analyser (SNA), Vector Network Analyser (VNA) & large signal network analyser which helps in measuring both phase & magnitude-based measurements.



Figure 3.16 Electrical Network Analyser

3.7 References

1. Dutrow, B. L., & Clark, C. M. (n.d.). X-ray Powder Diffraction (XRD).
2. Stanjek, H., & Häusler, W. (2004). Basics of X-ray Diffraction. *Springers series in plasma science and technology*.
3. Baskaran, S. (2010). Structure and Regulation of Yeast Glycogen Synthase.
4. Mabey, P. (2016). A study on dense plasmas using molecular dynamics and X-ray scattering techniques.
5. Unruh, D. K., Forbes, T. Z., Kenney, J. P., Veeramani, H., & Alessi, D. S. (2019). 9 - X-ray Diffraction Techniques. *Analytical Geomicrobiology*.
6. Mokobi, F. (2022). Scanning Electron Microscope (SEM)- Definition, Principle, Parts, Images.
7. Ul-Hamid, A. (2018). A Beginners' Guide to Scanning Electron Microscopy.
8. Worsfold, P. (2005). SPECTROPHOTOMETRY | Overview. *Encyclopedia of Analytical Science (Second Edition)*.
9. Tom, J. (2023). UV-Vis Spectroscopy: Principle, Strengths and Limitations and Applications.
10. Makuła, P., Makuła, P., & Macyk, W. (2018). How To Correctly Determine the Band Gap Energy of Modified Semiconductor Photocatalysts Based on UV–Vis Spectra.
11. Marcon, P., & Ostanina, K. (2012). Overview of Methods for Magnetic Susceptibility Measurement.
12. Heikkilä, M., & Karttunen, A. (2020). Superconducting Quantum Interference Device (SQUID).

13. Javier, J. (2014). An Introduction to Raman Spectroscopy: Introduction and Basic Principles.
14. Bumbrah, G. S., & Sharma, R. M. (2016). Raman spectroscopy – Basic principle, instrumentation and selected applications for the characterization of drugs of abuse. *Egyptian Journal of Forensic Sciences*.
15. Skoog, D. A., Holler, F. J., & Crouch, S. R. (2021). *Principles of Instrumental Analysis*. United States of America.
16. Smith, E., & Dent, G. (2019). *Modern Raman Spectroscopy: A Practical Approach*, Second Edition.
17. Dey, T. (2022). Microplastic pollutant detection by Surface Enhanced Raman Spectroscopy (SERS): a mini-review.
18. Pandey, D. K., Kagdada, H. L., Sanchora, P., & Singh, D. K. (2021). Overview of Raman Spectroscopy: Fundamental to Applications. *Modern Techniques of Spectroscopy*.
19. Uitert, L. G. (1956). Dielectric Properties of and Conductivity in Ferrites.
20. Kuru, M., Kuru, T. Ş., Karaca, E., & Bağcı, S. (2020). Dielectric, magnetic and humidity properties of Mg–Zn–Cr ferrites. *Journal of Alloys and Compounds*.

CHAPTER 4: RESULTS AND DISCUSSIONS

4.1 X-Ray Diffraction Analysis

The structural properties of Graphene Oxide and Zinc Ferrite Graphene Oxide nanocomposite were studied using an X-ray powder diffraction (XRD) analysis, conducted on Rigaku Smart Lab Diffractometer using Cu-K α radiation ($\lambda = 1.5418 \text{ \AA}$) as shown in figure 4.1.



Figure 4.1 Rigaku X-ray Diffractometer

The X-ray diffraction patterns and Williamson-Hall plots of the prepared samples are depicted in figure 4.2 as (a) GO, (b) ZnFe₂O₄, (c) ZnFe₂O₄/GO (1.6%), (d) ZnFe₂O₄/GO (2.5%), (e) ZnFe₂O₄/GO (3.6%). The structural parameters of all the samples are listed in Table 4.1. The XRD result indicated good crystalline nature and monophasic formation of both GO and ZnFe₂O₄/GO nanocomposites through the well-defined positions of the diffraction lines and relative intensities of all observed peaks.

The XRD of GO synthesised using Modified Hummers Method shows crystalline nature displaying a strong diffraction peak at $2\theta \sim 10^\circ$ corresponding to 0.88 nm d-spacing with an index plane of (001) which is in good agreement with the literatures [\[4,24,25,26,29\]](#) The d-spacing was calculated using Bragg's relation.^[2] The diffraction peaks at 2θ are attributed to reflection planes (220), (311), (222), (400), (422), (511) and (440) which confirms the formation of cubic spinel structure with space group Fd3m and is well supported by the literature reports. [\[4,20\]](#) The absence of any additional peaks indicates the formation of single phase with the most

intense peak observed at $\sim 35^\circ$ corresponding to (311) diffraction plane. These peaks are well determined and clearly show the polycrystalline nature of the ferrite.

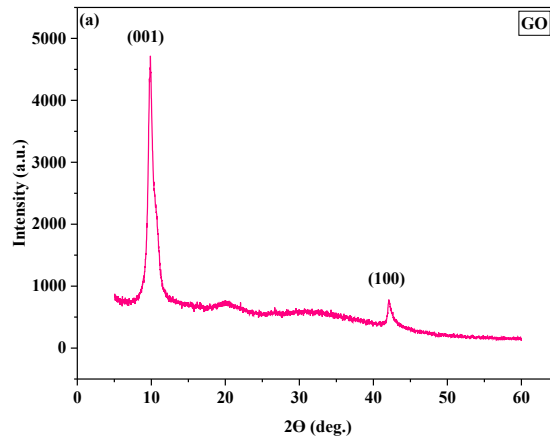


Figure 4.2(a) X-Ray Diffraction pattern of GO

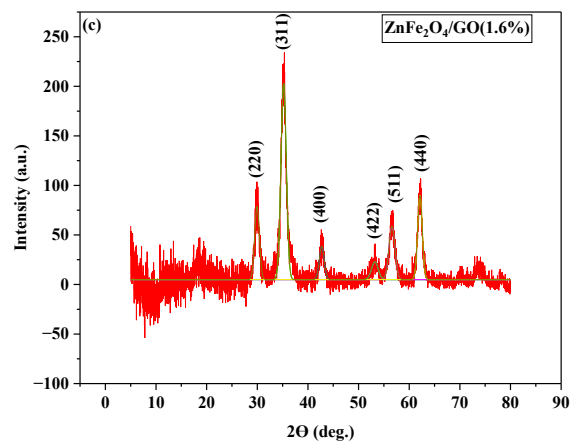
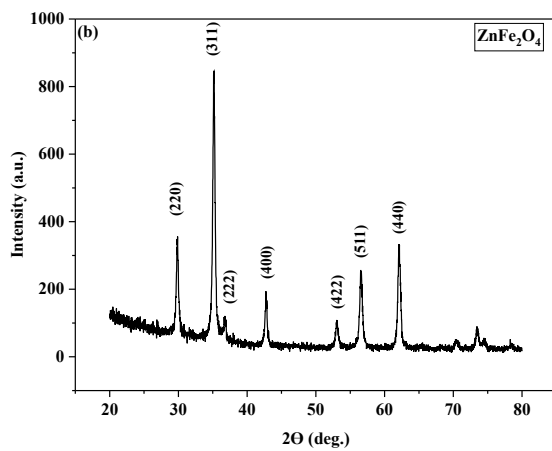


Figure 4.2(b) X-Ray Diffraction pattern of ZnFe_2O_4 , Figure 4.2(c) X-Ray Diffraction pattern of $\text{ZnFe}_2\text{O}_4/\text{GO}$ (1.6%)

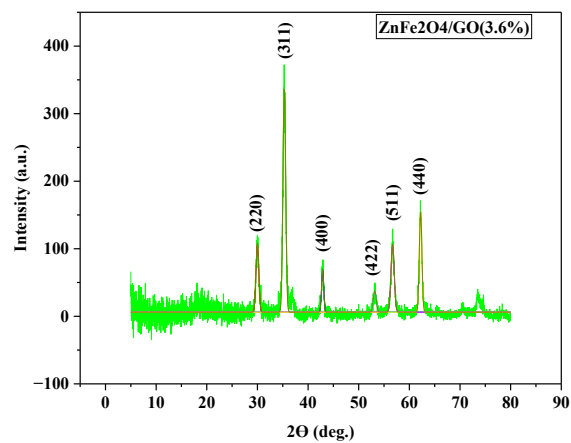
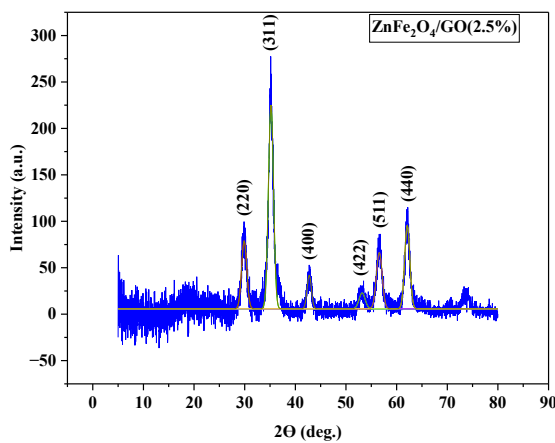


Figure 4.2(d) X-Ray Diffraction pattern of $\text{ZnFe}_2\text{O}_4/\text{GO}$ (2.6%), Figure 4.2(e) X-Ray Diffraction pattern of $\text{ZnFe}_2\text{O}_4/\text{GO}$ (3.6%)

Table 4.1 - Diffraction angle, Miller indices, interplanar spacing, lattice constant and strain of all the prepared samples of ZnFe₂O₄/GO [(a) ZnFe₂O₄ (b) ZnFe₂O₄/GO(1.6%), (c) ZnFe₂O₄/GO(2.5%), (d) ZnFe₂O₄/GO(3.6%)].

Table 4.1-(a) ZnFe₂O₄

Sr. No	2 Θ (Degrees)	Θ (Degrees)	(hkl) Miller Indices	d Interplanar spacing (Å)	a Lattice Constant (Å)
1	29.88	14.94	(220)	2.98	8.45
2	35.17	17.58	(311)	2.55	8.45
3	36.78	18.39	(222)	2.44	8.46
4	42.74	21.37	(400)	2.11	8.45
5	53.02	26.51	(422)	1.72	8.45
6	56.52	28.26	(511)	1.63	8.45
7	62.12	31.06	(440)	1.49	8.44

Average Lattice constant

= **8.45 Å**

Crystallite Size (311)

= **25.58 nm**

Table 4.1-(b) ZnFe₂O₄/GO (1.6%)

Sr. No	2 Θ (Degrees)	Θ (Degrees)	(hkl) Miller Indices	d Interplanar spacing (Å)	a Lattice Constant (Å)
1	29.92	14.96	(220)	2.98	8.44
2	35.36	17.68	(311)	2.54	8.41
4	62.64	21.32	(400)	2.12	8.47
5	53.28	26.64	(422)	1.72	8.41
6	56.5	28.25	(511)	1.63	8.45
7	62.26	31.13	(440)	1.49	8.42

Average Lattice constant

= **8.41 Å**

Crystallite Size (311)

= **7.03 nm**

Table 4.1-(c) ZnFe₂O₄/GO (2.5%)

Sr. No	2 Θ (Degrees)	Θ (Degrees)	(hkl) Miller Indices	d Interplanar spacing (Å)	a Lattice Constant (Å)
1	29.24	14.62	(220)	3.05	8.63
2	35.14	17.57	(311)	2.55	8.46
3	42.52	21.26	(400)	2.12	8.49
4	53	26.5	(422)	1.72	8.45
5	56.56	28.28	(511)	1.62	8.44
6	62.16	31.08	(440)	1.49	8.43

Average Lattice constant

= **8.46 Å**

Crystallite Size (311) =

7.43 nm

Table 4.1-(d) ZnFe₂O₄/GO (3.6%)

Sr. No	2 Θ (Degrees)	Θ (Degrees)	(hkl) Miller Indices	d Interplanar spacing (\AA)	a Lattice Constant (\AA)
1	29.88	14.94	(220)	2.98	8.45
2	35.27	17.64	(311)	2.54	8.43
4	42.94	21.47	(400)	2.10	8.42
5	53.2	26.6	(422)	1.72	8.42
6	56.72	28.36	(511)	1.62	8.42
7	62.18	31.09	(440)	1.49	8.44

Average Lattice constant

= **8.43 \AA**

Crystallite Size (311)

= **13.56 nm**

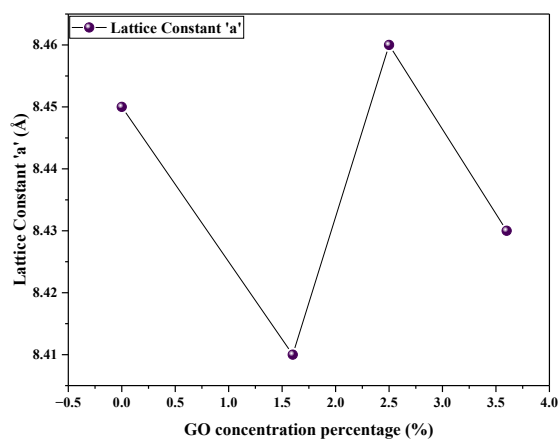


Figure 4.3 Lattice constant as a function of GO concentration

The interplanar spacing 'd' and the lattice parameter 'a' tabulated in table 4.1 were calculated using Bragg's condition. ^[31]

The evolution of the lattice parameter of the Zinc ferrite graphene oxide as a function of graphene oxide concentration is presented in figure 4.3. The lattice parameter was seen to vary between 8.41 \AA to 8.46 \AA with increase in GO concentration.

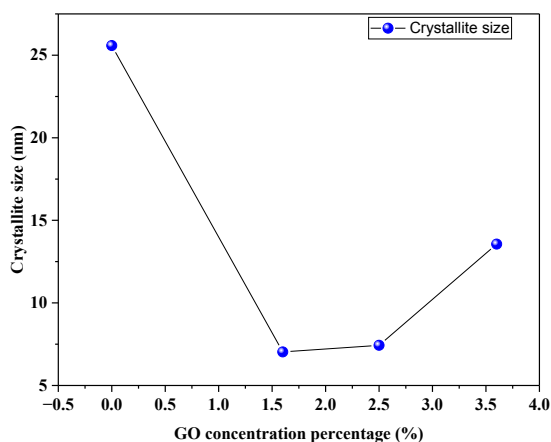


Figure 4.4 Crystallite Size ‘t’ as a function of GO concentration

The crystallite size of the nanocomposites was calculated using Debye Scherrer formula. ^[7]

Where D is the crystallite size, k is the Scherrer constant which equals to 0.94, represents wavelength of the Cu-K α radiation ($\lambda = 1.5418 \text{ \AA}$) and β is the Full Width Half Maximum of the most intense peak (311). Overall an increase was seen in the crystallite size of the ZnFe₂O₄/GO nanocomposite with increase in GO concentration. The variation of Crystallite size as a function of GO concentration is presented in figure 4.4.

4.2 Scanning Electron Microscope Analysis



Figure 4.5 Carl Zeiss Scanning Electron Microscope Setup

The morphology of the as prepared samples were studied using the Carl Zeiss Scanning Electron Microscope (SEM) as show in the figure 4.4. The SEM images were analysed using the ImageJ software and the average particle size of the as prepared samples was determined. The SEM images along with the histograms of particle size distribution along with SEM images are show in the figure 4.5. The average agglomeration size of the $\text{ZnFe}_2\text{O}_4/\text{GO}$ composites are listed in the table. We can see that the average agglomeration size decreases with the increase in graphene oxide concentration.

Figure shows the SEM images of as-synthesized ZnFe_2O_4 and the $\text{ZnFe}_2\text{O}_4/\text{GO}$ nanocomposites with GO concentration of 1.6%, 2.5%, 3.6% respectively. The $\text{ZnFe}_2\text{O}_4/\text{GO}$ nanocomposites showed considerably different morphological structure where ZnFe_2O_4 nanoparticles were found to be implanted on graphene oxide layers. Figure shows the as synthesised ZnFe_2O_4 nanoparticles that are small, spherical shaped particles that are densely packed together and uniformly distributed. Figure demonstrates the $\text{ZnFe}_2\text{O}_4/\text{GO}$ nanocomposites where it is observed that ZnFe_2O_4 nanoparticles are grafted on the layered structure of GO. The ZnFe_2O_4 particles in the $\text{ZnFe}_2\text{O}_4/\text{GO}$ nanocomposites, with GO concentration of 1.6% and 2.5%, were clumped in certain regions while the ZnFe_2O_4 particles in the $\text{ZnFe}_2\text{O}_4/\text{GO}$ nanocomposites, with GO concentration of 3.6% showed that the ZnFe_2O_4 particles were uniformly distributed over the GO layers.

The decrease in the average agglomeration size of the zinc ferrite graphene oxide nanocomposites with an increase in the concentration of graphene oxide indicates that graphene oxide is playing a role in controlling the size and morphology of the nanocomposites.^[28] Graphene oxide is a two-dimensional material with a high surface area, which can act as a template or a surface modifier for the growth of zinc ferrite nanoparticles.^[34] The presence of graphene oxide in the synthesis of nanocomposites can also improve the dispersion of nanoparticles, which can lead to a reduction in agglomeration

size.^[1] Furthermore, the decrease in agglomeration size of the nanocomposites can also have significant implications for their properties and applications.^[6] For example, a smaller agglomeration size can lead to an increase in surface area, which can enhance the reactivity and catalytic activity of the nanocomposites.^[5] The decrease in agglomeration size can also lead to changes in magnetic, electronic, and optical properties, which can be beneficial for various applications, such as sensors^[11], energy storage^[14], and catalysis.^[21]

In summary, the decrease in average agglomeration size of the zinc ferrite graphene oxide nanocomposites with an increase in graphene oxide concentration suggests that graphene oxide plays a significant role in controlling the size and morphology of the nanocomposite.

Table 4.2 Average agglomerate size of composites

Concentration	0.0	1.6	2.5	3.6
Agglomeration size (nm)	89	664	264	74

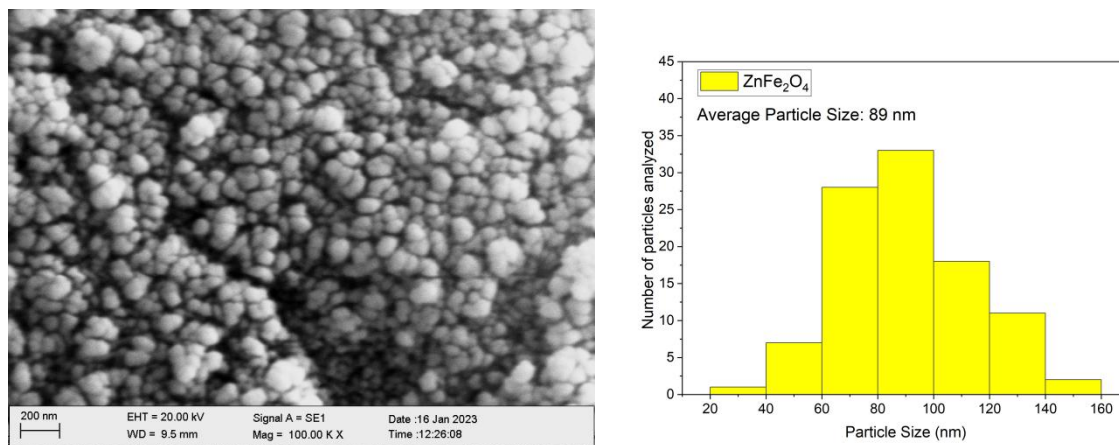


Figure 4.6 (a) SEM image and histogram of ZnFe₂O₄

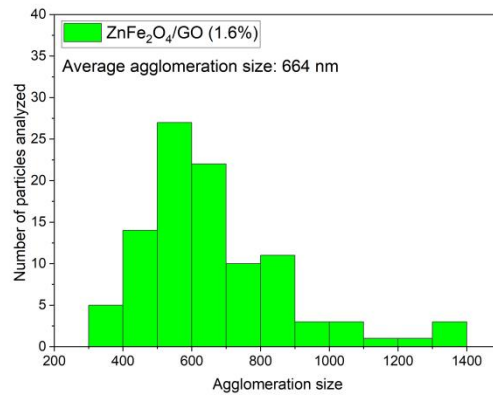
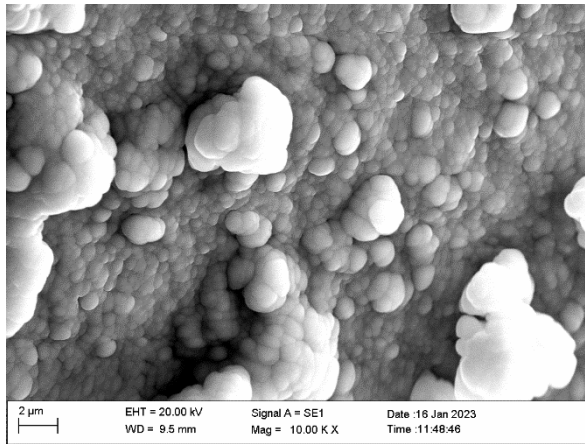


Figure 4.6 (b) SEM image and histogram of ZnFe₂O₄/GO (1.6%)

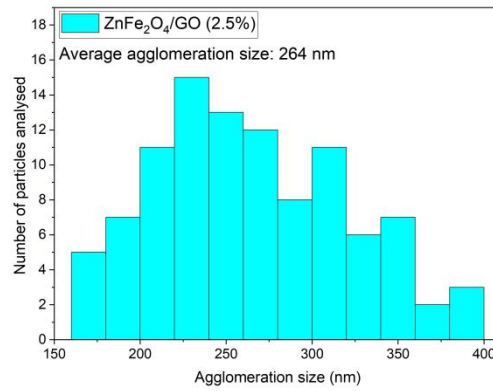
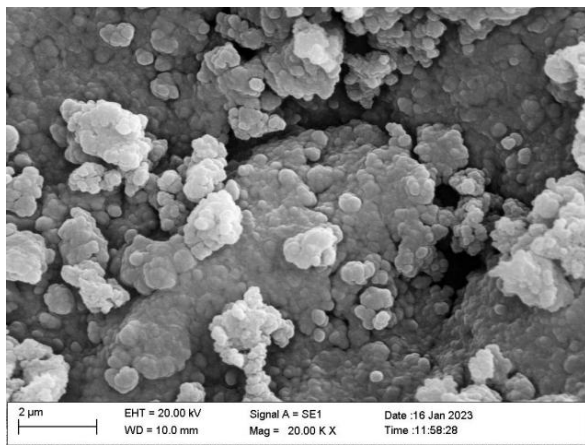


Figure 4.6 (c) SEM image and histogram of ZnFe₂O₄/GO (2.5%)

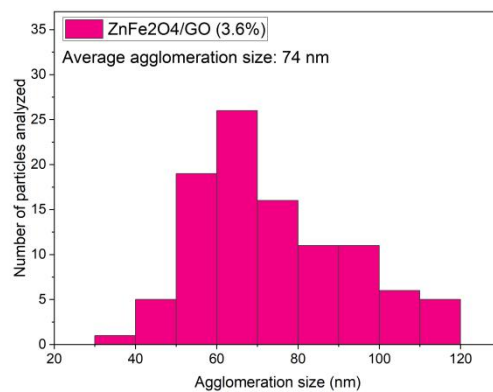
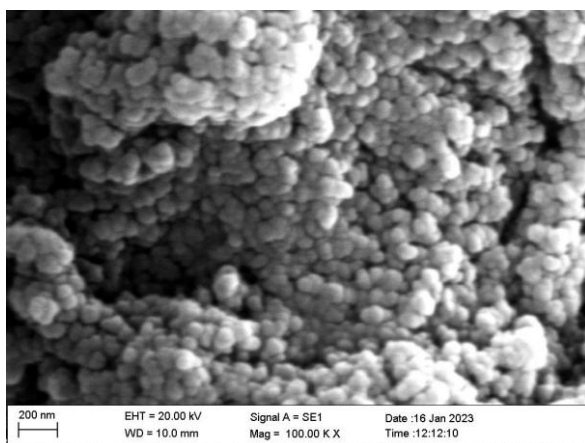


Figure 4.6 (d) SEM image and histogram of ZnFe₂O₄/GO (3.6%)

4.3 UV-Visible Diffusive Reflectance Spectroscopy Analysis



Figure 4.7 UV-Visible Spectrophotometer

UV-Visible spectra analysis was done using UV-Visible spectrometer, shown in the figure 4.6. From the Tauc's plot we can conclude that the band gap energy of the nanocomposites decreases as the concentration of Graphene Oxide increases. The Tauc's plots for the composites are shown in the figure 4.7

The band gap was calculated by using the Tauc's Plot. For UV- Visible diffuse reflectance Spectroscopy we replace the absorption coefficient (α) in the Tauc's Equation (equation 1) with the Kubelka-Munk Function i.e., $F(R)$ (equation 2), which is the ratio of the absorption coefficient (k) to the scattering coefficient (s) in m^{-1} .

$$(\alpha h\nu)^2 = A(h\nu - E_g) \quad \text{equation 1}$$

Where,

α is the absorption coefficient

h is the Planck's constant

ν is the photon's frequency

A is a proportionality constant

E_g is the band gap energy

γ denotes the nature of electronic transition

where $\gamma = 2$ for direct allowed transitions, $\gamma = 1/2$ for indirect allowed transitions,

$\gamma = 2/3$ for direct forbidden transitions, $\gamma = 1/3$ for indirect forbidden transitions

$$(F(R) - R)h\nu^\gamma = A(h\nu - E_g) \quad \text{equation 2}$$

Where,

$$F(R) = k/s = (1-R)^2 / 2R$$

R is the % reflectance obtained in the DRS data. The subscript ∞ denotes sufficient thickness of the sample layer that is thick enough to completely hide the support.

The observed reduction in energy band gap of Zinc ferrite/ graphene oxide nanocomposites, which occurs due to the introduction of additional energy states in the band gap region by the graphene oxide, suggests that it could act as a dopant and enhance the electrical conductivity of the nanocomposites.

This is a favourable characteristic for energy storage applications, as higher electrical conductivity can facilitate quicker charging and discharging rates and overall superior energy storage capabilities.^[7] Therefore, it can be inferred that the incorporation of graphene oxide in these nanocomposites could be a promising approach to improve their performance as energy storage materials.

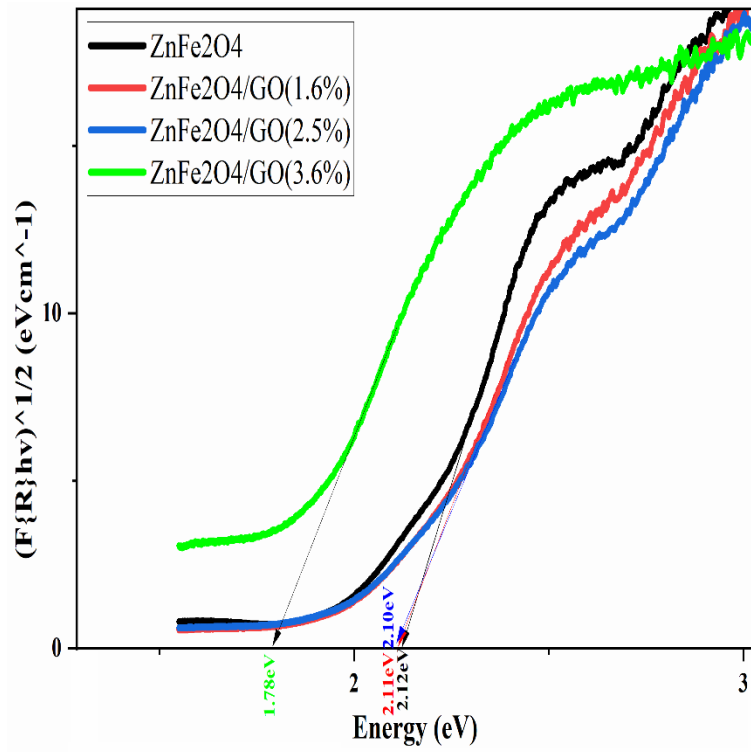


Figure 4.8 (a) ZnFe₂O₄ and all the composites

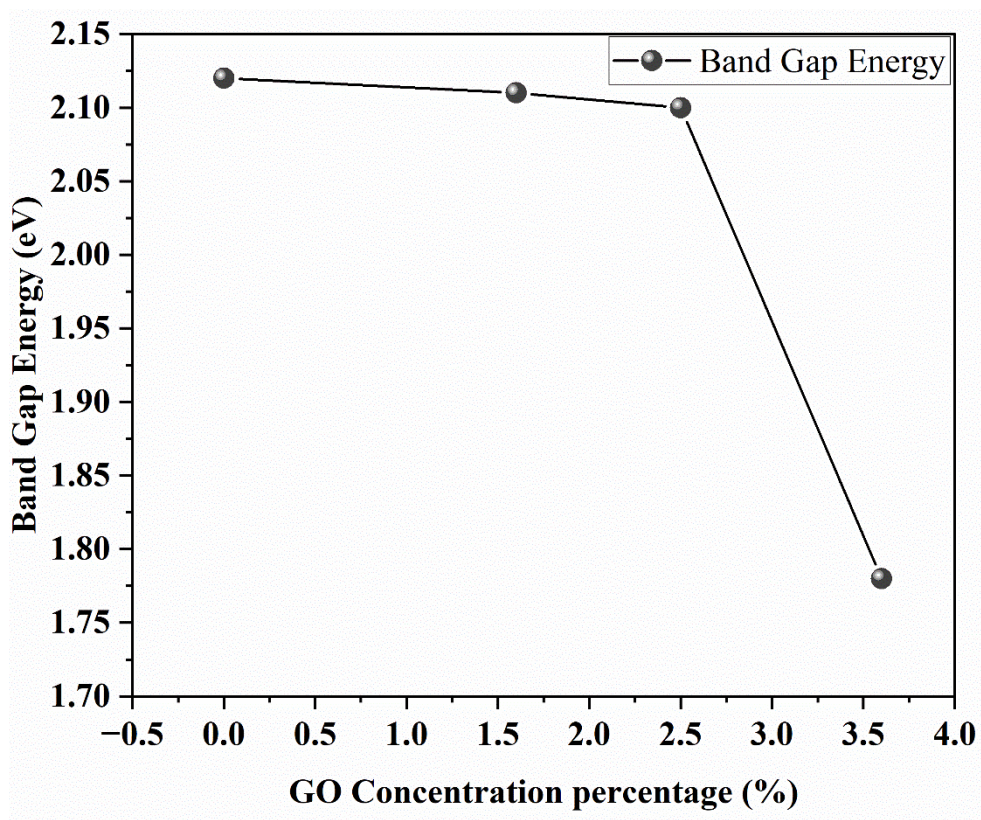


Figure 4.8 (b) Variation of Band Gap with GO concentration in the nanocomposite

4.4 The Superconducting Quantum Interference Device (SQUID) Analysis



Figure 4.8 SQUID magnetometer

Superconducting Quantum Interference Device (SQUID) measurements were conducted to study the magnetic properties of as-prepared samples of ZnFe_2O_4 , $\text{ZnFe}_2\text{O}_4/\text{GO}$ (1.6%), $\text{ZnFe}_2\text{O}_4/\text{GO}$ (2.5%), and $\text{ZnFe}_2\text{O}_4/\text{GO}$ (3.6%) using the Superconducting Quantum Interference Device shown in the figure 4.8. The hysteresis loop obtained from these measurements, which are shown in figure 4.9, depicts the relationship between magnetization intensity M and the applied magnetic field H . All the samples showed paramagnetic behaviour, but the magnetic moment increased with increasing graphene oxide concentration. This suggests that graphene oxide acts as a catalyst to improve the magnetic interactions between the zinc ferrite nanoparticles.^[12]

The high surface area of graphene oxide and its numerous oxygen-containing functional groups provide sites for the nucleation and growth of magnetic particles, leading to enhanced magnetic properties^[33]. Additionally, the interaction between graphene oxide and zinc ferrite

nanoparticles facilitates the formation of a well-dispersed and homogeneously distributed composite structure, further enhancing the magnetic properties of the nanocomposites.^[19]

From the results of the SQUID analysis, it can be concluded that incorporating graphene oxide into zinc ferrite nanocomposites can enhance their magnetic properties. This improvement has potential applications in various fields, including magnetic data storage^[17], biomedical imaging^[10], and catalysis.^[35]

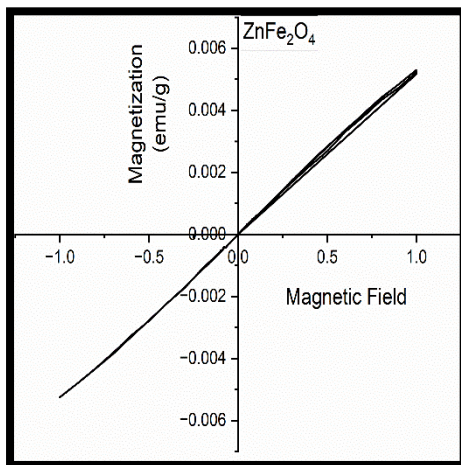


Figure 4.10 (a) ZnFe₂O₄

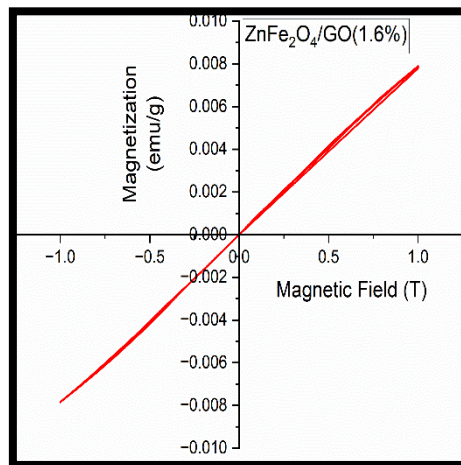


Figure 4.10 (b) ZnFe₂O₄/GO(1.6%)

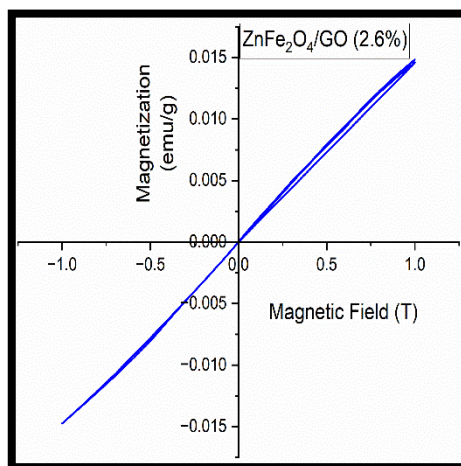


Figure 4.10 (c) ZnFe₂O₄/GO(2.5%)

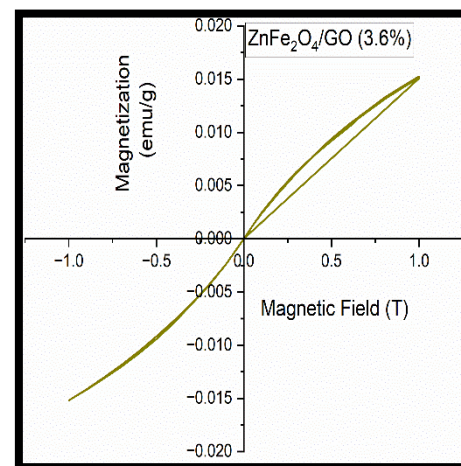


Figure 4.10 (d) ZnFe₂O₄/GO(1.6%)

4.5 Raman Spectroscopy Analysis



Figure 4.11 LabRAM HR Evolution Raman Microscope

The Raman Spectra of the as prepared samples were acquired using the LabRAM HR Evolution Raman Microscope which is shown in figure 4.11. The Raman spectroscopy of graphene oxide showed two prominent peaks known as the D band and G band. The Raman spectroscopy of pure ZnFe_2O_4 showed two F_{2g} and A_{1g} bands. In the nanocomposites of Zinc Ferrite Graphene Oxide, the D and G bands appear to be shifted when compared to the peaks obtained in Graphene Oxide.

In Graphene Oxide, the D band arises due to defects and disorder in the graphene structure, while the G band corresponds to the first-order scattering of sp^2 -bonded carbon atoms.^[2] For ZnFe_2O_4 , The F_{2g} band is a high-frequency band that is associated with the stretching vibration of the oxygen octahedra in the spinel structure of ZnFe_2O_4 , while the A_{1g} band is a low-frequency band that is associated with the bending vibration of the oxygen octahedra.^[13] The shift in the D and G bands in the Raman spectrum of zinc ferrite graphene oxide nanocomposites could be due to the interaction between the graphene oxide and zinc ferrite nanoparticles. The presence of zinc ferrite nanoparticles in the nanocomposite could cause changes in the electron density and bonding environment of the graphene oxide sheets,

leading to changes in the position and intensity of the D and G bands.^[18] Several studies have reported similar shifts in the Raman bands of graphene-based nanocomposites due to the interaction with other materials. For example, a study by Liu et al. (2018) reported a shift in the D and G bands of reduced graphene oxide-nickel oxide nanocomposites due to the interaction between the graphene oxide and nickel oxide nanoparticles.^[16]

Another study by Haldar et al. (2020) reported a shift in the D and G bands of graphene oxide-magnetite nanocomposites due to the interaction between the graphene oxide and magnetite nanoparticles. The authors attributed the shift to the charge transfer between the graphene oxide and magnetite nanoparticles^[9]

Therefore, the shift in the D and G bands in the Raman spectrum of zinc ferrite graphene oxide nanocomposites could be due to similar interactions between the graphene oxide and zinc ferrite nanoparticles, leading to changes in the electron density and bonding environment of the graphene oxide sheets. Further studies could be carried out to confirm this and investigate the nature of the interaction in more detail

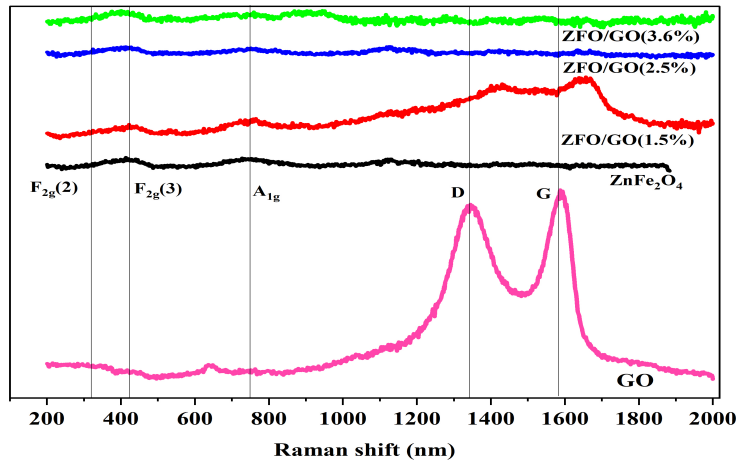


Figure 4.12 GO, ZnFe_2O_4 and all composites

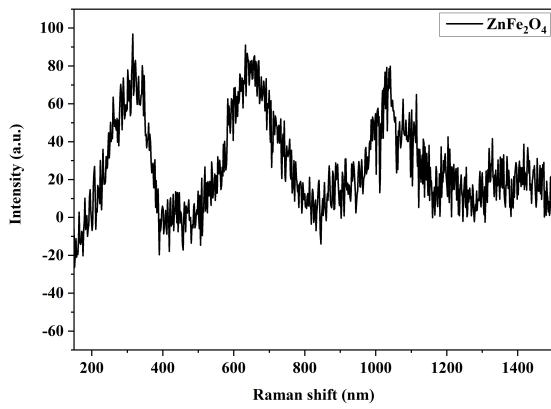


Figure 4.12 (a) ZnFe_2O_4

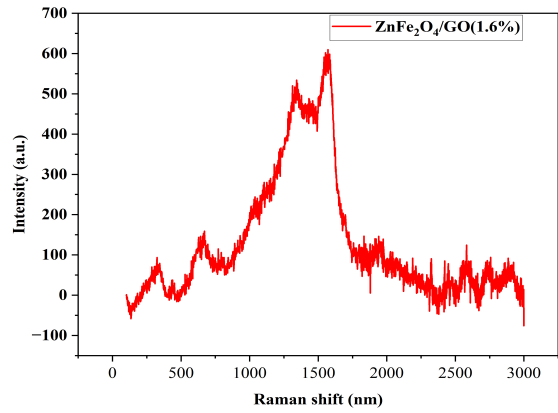


Figure 4.12 (b) $\text{ZnFe}_2\text{O}_4/\text{GO}(1.6\%)$

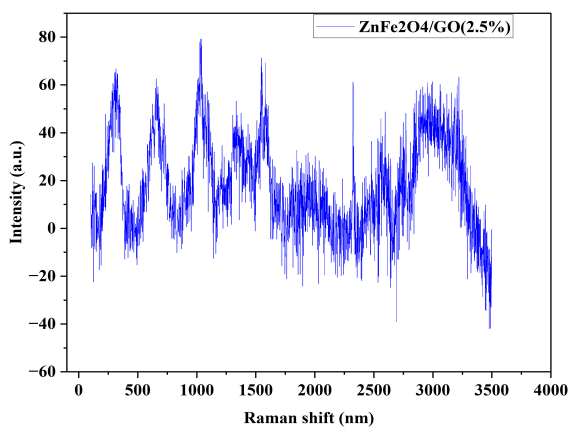


Figure 4.12(c) $\text{ZnFe}_2\text{O}_4/\text{GO}(2.5\%)$

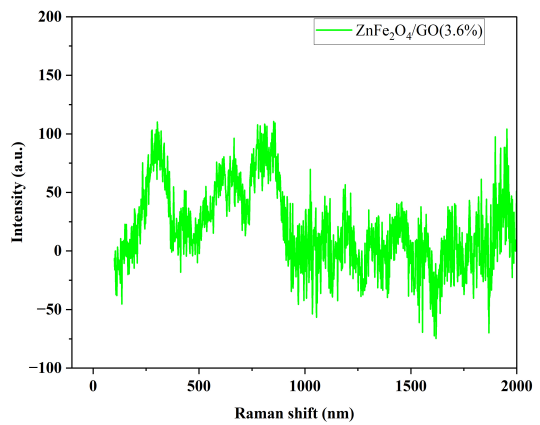


Figure 4.12(d) $\text{ZnFe}_2\text{O}_4/\text{GO}(1.6\%)$

4.6 Electrical Analysis by Network Analyser

The electrical analysis was conducted using the LCR meter as shown in the figure 4.12. In order to perform electrical investigations, depending on the frequency, the disk shaped samples were painted with porous silver electrodes on both sides. Impedance spectroscopy is a critical method in the investigation of the electrical properties of materials. The reason is that, the conductivity of a material can be a separate contribution of the grains, grain boundaries and electrodes, or they may all contribute to the combination of these compounds.^[30]



Figure 4.13: Network Analyser Set-up

4.6.1 Variation of Dielectric constant with Frequency

The dielectric constant values of the as prepared samples were plotted as a function of frequency as shown in figure 4.13. The dielectric constant for lower frequencies was seen to be increasing with increasing graphene oxide concentration in the nanocomposite. It can be seen that the sample with maximum graphene oxide concentration, i.e., $\text{ZnFe}_2\text{O}_4/\text{GO}$ (3.6%) has a very high value of dielectric constant as compared to the other samples. The dielectric constant was seen to be decreasing further with increasing frequency. The increase in dielectric constant with increasing graphene oxide concentration suggests that the incorporation of graphene oxide has a significant impact on the electrical properties of the nanocomposite material as the high surface area and numerous oxygen containing functional

groups of graphene oxide can introduce additional energy states in the band gap region of the nanocomposite material. This can lead to an increase in the dielectric constant, which is a measure of a material's ability to store electrical energy in an electric field. The introduction of graphene oxide into a nanocomposite can also improve the dispersion of nanoparticles, leading to a reduction in agglomeration size and increased interfacial contact between the particles. This improved dispersion can further enhance the electrical properties of the material. [3] This information could be useful in designing and optimizing the material for specific energy storage or other electrical applications, by controlling the concentration of graphene oxide to achieve the desired dielectric properties. [23]

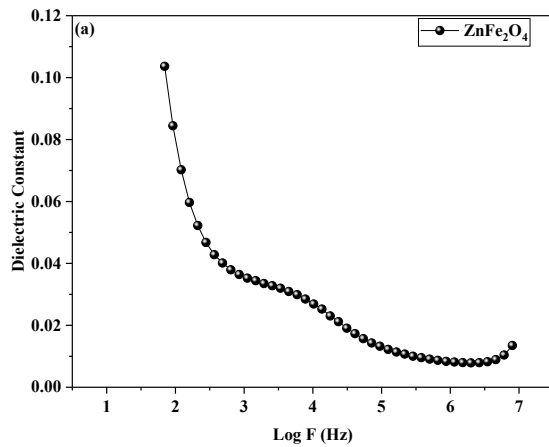


Figure 4.14(a) ZnFe₂O₄

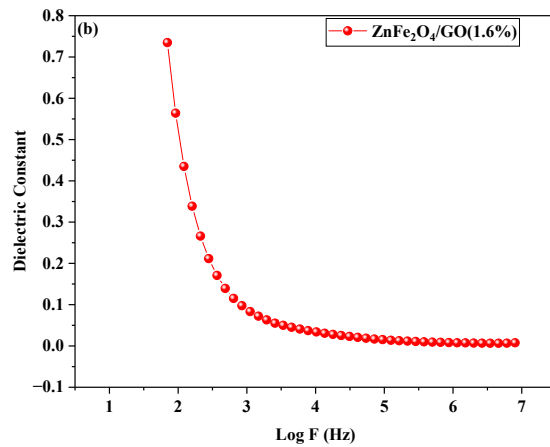


Figure 4.14(b) ZnFe₂O₄/GO(1.6%)

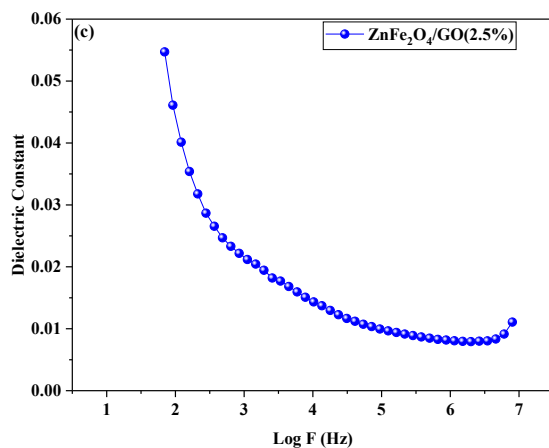


Figure 4.14(c) ZnFe₂O₄/GO(2.5%)

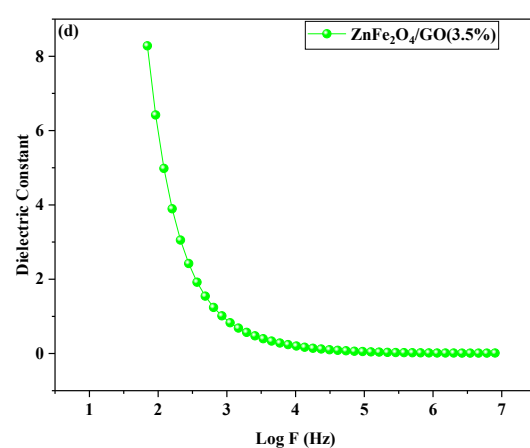


Figure 4.14(d) ZnFe₂O₄/GO(3.6%)

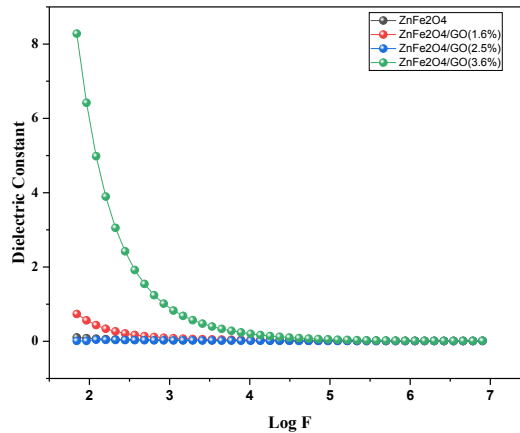


Figure 4.14(d) ZnFe₂O₄ and the as prepared composites

4.6.2 Variation of Dielectric loss with Frequency

The dielectric loss values of the as prepared samples of ZnFe₂O₄ and ZnFe₂O₄/GO nanocomposites were plotted against the frequency as shown in figure 4.14. It was observed that these nanocomposites had low dielectric loss values, which increased with an increase in the concentration of graphene oxide.

The observation of low dielectric loss values in the zinc ferrite graphene oxide nanocomposites suggests that the material has high electrical insulation properties, as it is able to minimize the dissipation of electrical energy in the form of heat.^[27] This can be beneficial for a variety of electrical and electronic applications, where high levels of electrical insulation and low energy losses are desirable, such as in capacitors, insulators, and other components.^[15] Additionally, the low dielectric loss values may also indicate that the material has good stability and resistance to electrical breakdown, as well as high durability and longevity.^[32]

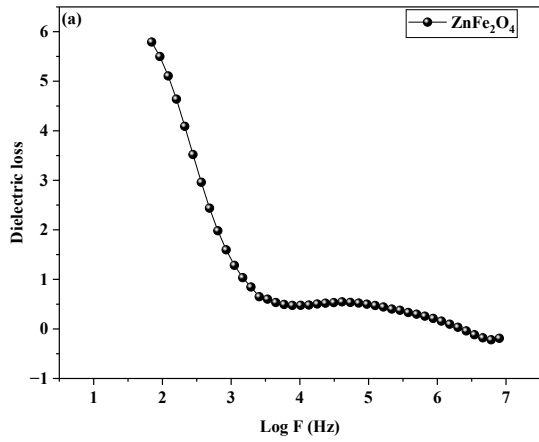


Figure 4.15(a) ZnFe_2O_4

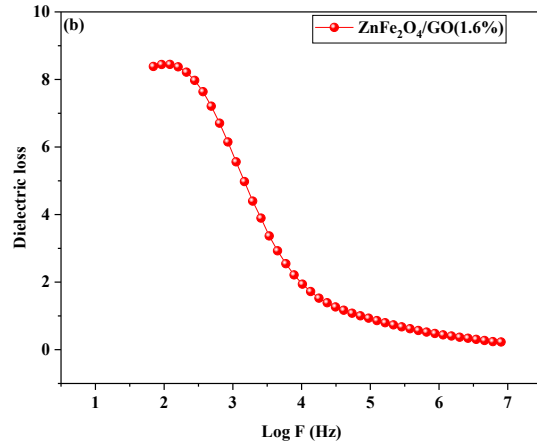


Figure 4.15(b) $\text{ZnFe}_2\text{O}_4/\text{GO}(1.6\%)$

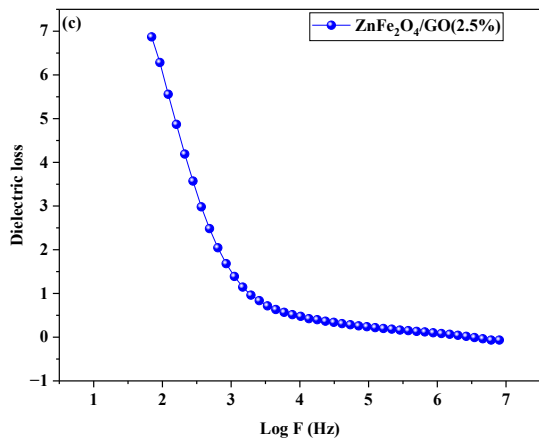


Figure 4.15(c) $\text{ZnFe}_2\text{O}_4/\text{GO}(2.5\%)$

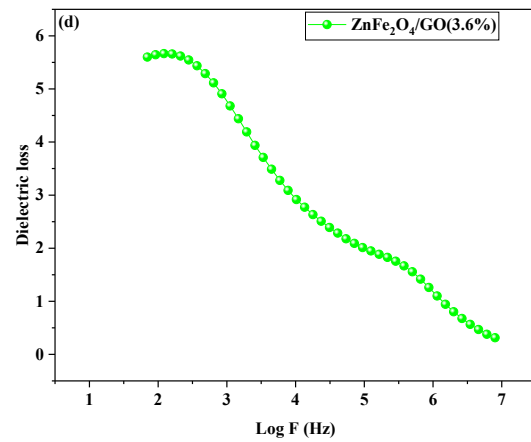


Figure 4.15(d) $\text{ZnFe}_2\text{O}_4/\text{GO}(3.6\%)$

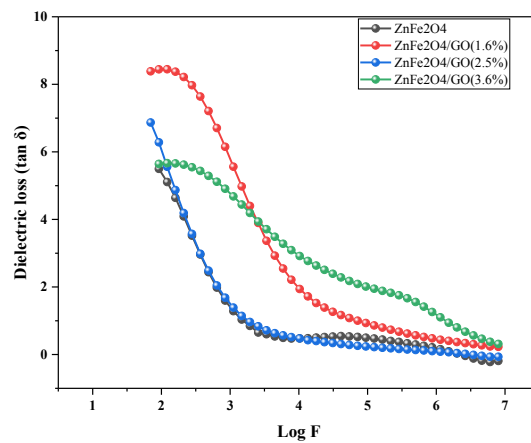


Figure 4.15(e) ZnFe_2O_4 and its composites

4.6.3 Nyquist's Plots

The figure depicts the Nyquist plots, which illustrates the relationship between imaginary impedance and real impedance. Nyquist plots show two semicircles, revealing the presence of single relaxation processes in material with lower concentrations of GO associated with grains and grain boundaries. The sample $\text{ZnFe}_2\text{O}_4/\text{GO}$ (3.6%) was seen to exhibit several relaxation processes and can be modelled by an electrical equivalent circuit composed of three series sets of resistance and capacitance in parallel. The microstructural effect is considered the most significant factor that influences the impedance and relaxation processes of ferrites. Ferrite materials are believed to be made up of crystal microstructures that are stacked on top of each other, and these microstructures contain conductive grains that are separated by resistant grain boundaries.^[8]

The observation of two semicircles in the Nyquist plot for the sample $\text{ZnFe}_2\text{O}_4/\text{GO}$ (3.6%) suggests that there may be two relaxation processes occurring in the material. These additional relaxation processes could affect the electrical conductivity, dielectric properties, and energy storage capacity of the material, which could have implications for its performance in energy storage applications.

Furthermore, the concentration of graphene oxide in the nanocomposite can affect the morphology, microstructure, and interfacial properties of the material, which can also impact its energy storage properties.^[22] Therefore, understanding the relaxation processes and microstructural effects of zinc ferrite and graphene oxide nanocomposites is crucial to optimizing their performance for energy storage applications.

Further research is needed to fully understand the relationship between the graphene oxide concentration and the relaxation processes in the nanocomposites, and to explore their potential for practical applications in energy storage devices.

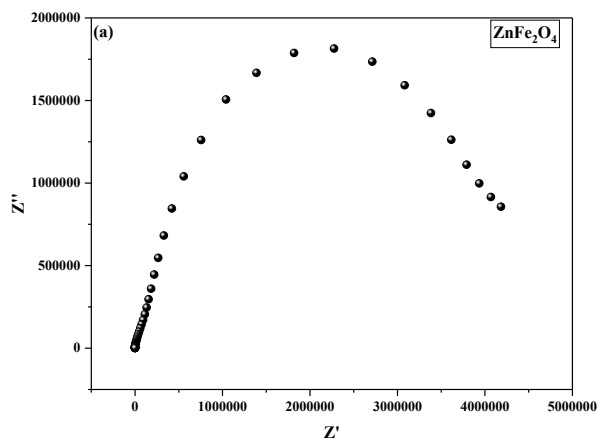


Figure 4.16 (a) ZnFe_2O_4

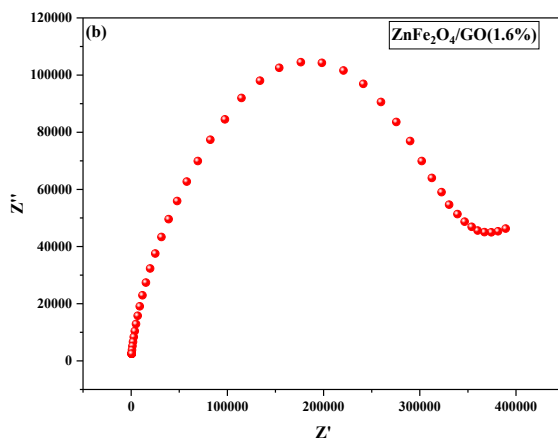


Figure 4.16 (b) $\text{ZnFe}_2\text{O}_4/\text{GO}(1.6\%)$

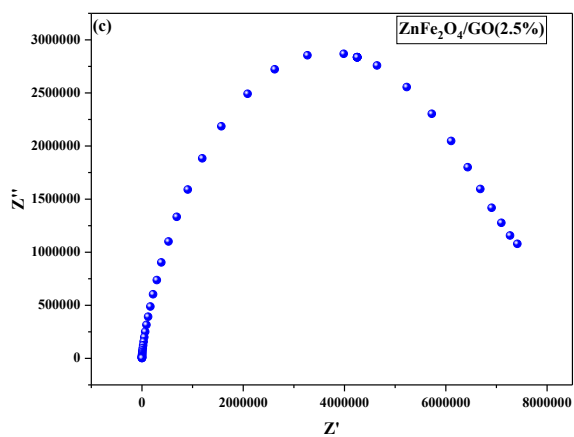


Figure 4.16 (c) $\text{ZnFe}_2\text{O}_4/\text{GO}(2.5\%)$

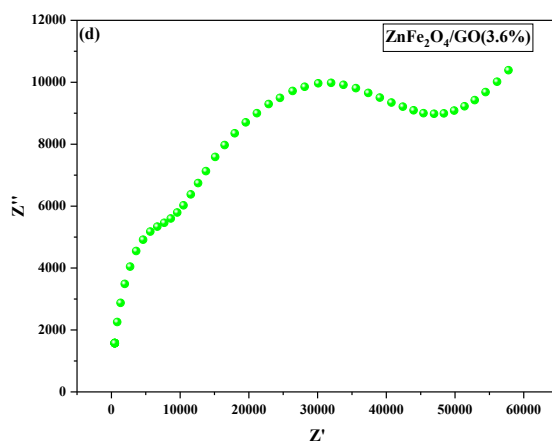


Figure 4.16 (d) $\text{ZnFe}_2\text{O}_4/\text{GO}(3.6\%)$

4.7 References

1. Irfan, S., Liang, G., Li, F., Chen, Y., Rizwan, S., Jin, J., Zhuanghao, Z., & Ping, F. (2019). Effect of Graphene Oxide Nano-Sheets on Structural, Morphological and Photocatalytic Activity of BiFeO₃-Based Nanostructures. *Nanomaterials*, 9(9), 1337.
2. A. C. Ferrari and J. Robertson titled "Interpretation of Raman spectra of disordered and amorphous carbon" (2000)
3. Adaval, A., Subash, C. K., Shafeeq, V. H., Singh, S., Maji, P. K., Aslam, M., Turney, T. W., Simon, G. P., & Bhattacharyya, A. R. (2022). Exploring interfacial interactions, dielectric, ferroelectric and piezoelectric properties of ultrahigh molecular weight polyethylene/graphene oxide nanocomposites. *Composites Science and Technology*, 219, 110130.
4. Bhattacharyya, R., Prakash, O., Roy, S., Singh, A. P., Bhattacharya, T. K., Maiti, P., . . . Das, S. (2019). Graphene oxide-ferrite hybrid framework as enhanced broadband absorption in gigahertz frequencies.
5. Dou, P., Tan, F., Wang, W., Sarreshteh, A., Qiao, X., Qiu, X., & Chen, J. (2019). One-step microwave-assisted synthesis of Ag/ZnO/graphene nanocomposites with enhanced photocatalytic activity. *Applied Surface Science*, 487, 555-564. doi: 10.1016/j.apsusc.2019.05.207.
6. Miller, D. R., Akbar, S. A., & Morris, P. A. (2018). Nanoscale metal oxide-based heterojunctions for gas sensing: A review. *Sensors and Actuators B: Chemical*, 255, 3313-3348. doi: 10.1016/j.snb.2017.09.096.

7. Yao, X., Kong, J., Zhou, D., Zhao, C., Zhou, R., & Lu, X. (2016). Mesoporous zinc ferrite/graphene composites: Towards ultra-fast and stable anode for lithium-ion batteries. *Electrochimica Acta*, 190, 929-935. doi: 10.1016/j.electacta.2016.01.088.
8. Wang, X., Zhang, H., Shi, L., Li, J., Jin, L., Cheng, L., Jia, L., Peng, R., & Zhang, D. (2019). Synthesis of low-temperature sintered M-type barium ferrites with enhanced microstructure, magnetic and dielectric properties. *Journal of Alloys and Compounds*, 798, 757-763.
9. Tanwar, S., & Mathur, D. (2017). Magnetite-graphene oxide nanocomposites: Facile synthesis and characterization of optical and magnetic property. *Journal of Magnetism and Magnetic Materials*, 439, 48-54.
10. Al-Rawashdeh, N. A. F., Allabadi, O., & Aljarrah, M. T. (2020). Photocatalytic Activity of Graphene Oxide/Zinc Oxide Nanocomposites with Embedded Metal Nanoparticles for the Degradation of Organic Dyes. *ACS Omega*, 5(43), 28046-28055.
11. Venugopal, A. P., Cespedes, O., & Russell, S. J. (2014). Controlling Dielectric and Magnetic Properties of PVdF/Magnetite Nanocomposite Fibre Webs. *Journal of Nanomaterials*, 2014, 1-9. doi: 10.1155/2014/145984.
12. Ali, R., Aziz, M. H., Gao, S., Khan, M. I., Li, F., Batool, T., Shaheen, F., & Qiu, B. (2019). Graphene oxide/zinc ferrite nanocomposite loaded with doxorubicin as a potential theranostic medium in cancer therapy and magnetic resonance imaging. *Materials Science and Engineering: C*, 99, 775-784.
13. Amiri, M., Salavati-Niasari, M., Akbari, A., & Razavi, R. (2014). Sol-gel auto-combustion synthesize and characterization of a novel anticorrosive cobalt ferrite

- nanoparticles dispersed in silica matrix. *Journal of Alloys and Compounds*, 592, 164-169.
14. Lou, Y., Liang, J., Peng, Y., & Chen, J. (2014). Ultra-small Co₃O₄ nanoparticles–reduced graphene oxide nanocomposite as superior anodes for lithium-ion batteries. *Journal of Materials Chemistry A*, 2(5), 1321-1327.
 15. Chee, W. K., Lim, H. N., Harrison, I., Chong, K. F., Zainal, Z., Ng, C. H., & Huang, N. M. (2017). Performance of Flexible and Binderless Polypyrrole/Graphene Oxide/Zinc Oxide Supercapacitor Electrode in a Symmetrical Two-Electrode Configuration. *Journal of Electronic Materials*, 46(6), 3486-3493
 16. Roychoudhury, A., Prateek, A., Basu, S. et al. Preparation and characterization of reduced graphene oxide supported nickel oxide nanoparticle-based platform for sensor applications. *J Nanopart Res* 20, 70 (2018).
 17. M. C. Daniel and D. Astruc, "Gold Nanoparticles: Assembly, Supramolecular Chemistry, Quantum-Size-Related Properties, and Applications toward Biology, Catalysis, and Nanotechnology," *Chemical Reviews*, vol. 104, pp. 293-346, 2004.
 18. Kooti, M., Naghdi Sedeh, A., Gheisari, Kh., & Figuerola, A. (2016). Synthesis, characterization, and performance of nanocomposites containing reduced graphene oxide, polyaniline, and cobalt ferrite. *Materials Chemistry and Physics*, 177, 415-423. doi: 10.1016/j.matchemphys.2016.04.035.
 19. Mallick, A., Mahapatra, A. S., Mitra, A., Greneche, J. M., Ningthoujam, R. S., & Chakrabarti, P. K. (2017). Magnetic properties and bio-medical applications in hyperthermia of lithium zinc ferrite nanoparticles integrated with reduced graphene oxide. *Journal of Magnetism and Magnetic Materials*, 429, 82-89.

20. Patar, S., Bhuyan, D. B., Konwar, M., Mahanta, B., Saikia, P., Guha, D. A., & Borthakur, D. L. (2022). Novel Zinc Ferrite Anchored Graphene Oxide Magnetic Nanocomposite for Photocatalytic Degradation of Textile Dyes.
21. Wang, L., & Gao, L. (2008). Morphology-Controlled Synthesis and Magnetic Property of Pseudocubic Iron Oxide Nanoparticles. *Journal of Physical Chemistry C*, 112(26), 9868-9873.
22. Nawaz, M., Islam, M. U., Nazir, M. A., Bano, I., Gul, I. H., & Ajmal, M. (2022). Transport properties in spinel ferrite/graphene oxide nanocomposites for electromagnetic shielding. *Journal of Alloys and Compounds*, 902, 162045.
23. Ishaq, S., Kanwal, F., Atiq, S., Moussa, M., Azhar, U., Gul, I., & Losic, D. (2021). Dielectric and impedance spectroscopic studies of three phase graphene/titania/poly(vinyl alcohol) nanocomposite films. *Applied Surface Science*, 536, 147932.
24. Sharma, N., Sharma, V., Jain, Y., Kumari, M., Gupta, R., Sharma, S. K., & Sachdev, K. (2017). Synthesis and Characterization of Graphene Oxide (GO) and Reduced Graphene Oxide (rGO) for Gas Sensing Application. *Macromolecular Symposia*.
25. Sharma, N., Sharma, V., Vyas, R., Kumari, M., Kaushal, A., Gupta, . . . Sachdev, K. (2019). A new sustainable green protocol for production of reduced graphene oxide and its gas sensing properties. *Journal of Science: Advanced Materials and Devices*.
26. Sohail, M., Saleem, M., Ullah, S., Saeed, N., Afridi, A., Khan, M., & Arif, M. (2017). Modified and improved Hummer's synthesis of graphene oxide for capacitors applications. *Modern Electronic Materials*.

27. Yao, X., Kong, J., Zhou, D., Zhao, C., Zhou, R., & Lu, X. (2022). Mesoporous zinc ferrite/graphene composites: Towards ultra-fast and stable anode for lithium-ion batteries. *Journal of Alloys and Compounds*, 900, 162866.
28. Meidanchi, A., & Mirabi, S. (n.d.). Comparison of Magnetic, Optical and Morphological Properties of the Nanocomposite of Reduced Graphene Oxide Coated with Zinc Ferrite Synthesized by One-Step Hydrothermal and Two-Step Sol-Gel / Hydrothermal Methods. Research Article.
29. Syed Nasimul Alam, N. S. (2017). Synthesis of Graphene Oxide (GO) by Modified Hummers Method and Its Thermal Reduction to Obtain Reduced Graphene Oxide (rGO).
30. Liu, S., Xue, S., Zhang, W., & Zhai, J. (2014). Enhanced dielectric and energy storage density induced by surface-modified BaTiO₃ nanofibers in poly(vinylidene fluoride) nanocomposites. *Ceramics International*, 40(10), 15633-15640.
31. Tirupanyama, B. V., Srinivas, C., Meena, S. S., Yusuf, S. M., Kumar, A. S., L., D., & Seshubai, V. (2015). Investigation of Structural and Magnetic Properties of co-precipitated. *Journal of Magnetism and Magnetic Materials*.
32. Wang, L., Wu, P., Cai, Y., Liao, X., Cao, M., & Yang, Y. (2017). Enhanced dielectric properties and energy storage performance of barium strontium titanate/polyvinylidene fluoride composites with core-shell structured conductive polymer-coated BaTiO₃ nanoparticles. *Journal of Materials Chemistry C*, 5(5), 1205-1217. doi: 10.1039/C6TC05048K

33. Sammaiah, A., Huang, W., & Wang, X. (n.d.). Synthesis of magnetic Fe₃O₄/graphene oxide nanocomposites and their tribological properties under magnetic field. *Journal of Magnetism and Magnetic Materials*.
34. Li, W., Zhang, J., Zhu, W., Qin, P., Zhou, Q., Lu, M., Zhang, X., Zhao, W., Zhang, S., & Cai, Z. (2019). Facile preparation of reduced graphene oxide/ZnFe₂O₄ nanocomposite as magnetic sorbents for enrichment of estrogens. *Journal of Colloid and Interface Science*, 534, 134-143..
35. Shu, R., Zhao, C., Zhang, J., Liu, W., Cao, X., Li, Y., & Liu, S. (2019). Facile synthesis of nitrogen-doped reduced graphene oxide/nickel ferrite hybrid nanocomposites with superior electromagnetic wave absorption performance in the X-band. *Journal of Alloys and Compounds*, 804, 342-352..

Chapter 5: CONCLUSION

In this study we have prepared ZnFe₂O₄/GO nanocomposites and investigated the effect on various structural, magnetic, optical and electrical properties of ZnFe₂O₄/GO nanocomposites.

GO was synthesised using Modified Hummers method. ZnFe₂O₄ nanoparticles were prepared using Hydrothermal method by including GO in hydrothermal matrix. Nanocomposites were prepared with three different concentrations of GO (50mg, 75mg and 100mg). Pure GO, ZnFe₂O₄ and nanocomposite samples were characterized using XRD, Raman spectroscopy, UV-visible spectroscopy, SEM, SQUID and Network analyser.

The XRD data showed the formation of pure GO, ZnFe₂O₄ and nanocomposites without any impurity phases. The lattice constant was found to be 8.45 Å for pure ZnFe₂O₄ and for nanocomposites the lattice constant was seen to vary from 8.41 Å to 8.46 Å. The crystallite size was seen to reduce from 25 nm for pure ZnFe₂O₄ to 7 nm for nanocomposites. Also, a marginal increase in crystallite size was observed for nanocomposites with increasing GO concentration.

The UV reflectance spectra showed reduction in band gap from 2.12 eV to 1.78 eV with increasing GO concentration.

Raman spectra showed presence of D and G bands for GO and F_{2g}(2), F_{2g}(3), A_{1g} bands for pure ZnFe₂O₄. The nanocomposite spectra contained all the characteristic bands of ZnFe₂O₄ and GO indicating formation of nanocomposites. However, a shift in the D and G band of GO was seen in the nanocomposites.

The morphology of nanocomposites was analysed using SEM which showed reduction in agglomeration with increasing GO concentration.

Magnetic properties illustrated using SQUID showed that samples exhibit paramagnetic behaviour. However, a marginal increase in magnetic moment was seen with increasing GO concentration.

Electrical properties such as Dielectric constant, Dielectric loss and impedance were measured using network analyser. Dielectric constant was seen to increase with GO concentration and showed a drastic increase for 100mg GO concentration. The Nyquist plots indicated reduction in impedance with graphene oxide concentration.